# Long range mutual activation establishes Rho and Rac polarity during cell migration

**Henry De Belly[1,2], Andreu Fernandez Gallen[3], Evelyn Strickland[1,2], Dorothy C. Estrada[1,2], Patrick J. Zager[1,2], Janis K Burkhardt[4,5], Hervé Turlier[3,4]✉, and Orion D. Weiner[1,2]✉**

[1]Cardiovascular Research Institute, University of California, San Francisco, San Francisco, CA, USA.
[2]Department of Biochemistry and Biophysics, University of California, San Francisco, San Francisco, CA, USA.
[3]Center for Interdisciplinary Research in Biology (CIRB), College de France, CNRS, INSERM, Universite PSL, Paris, France
[4]Department of Pathology and Laboratory Medicine, Children's Hospital of Philadelphia Research Institute, Philadelphia, PA
[5]Perelman School of Medicine, University of Pennsylvania, Philadelphia, PA, Philadelphia

**In migrating cells, the GTPase Rac organizes a protrusive front, whereas Rho organizes a contractile back. How these GTPases are appropriately positioned at the opposite poles of a migrating cell is unknown. Here we leverage optogenetics, manipulation of cell mechanics, and mathematical modeling to reveal a surprising long-range mutual activation of the front and back polarity programs that complements their well-known local mutual inhibition. This long-range activation is rooted in two distinct modes of mechanochemical crosstalk. Local Rac-based protrusion stimulates Rho activation at the opposite side of the cell via membrane tension-based activation of mTORC2. Conversely, local Rho-based contraction induces cortical-flow-based remodeling of membrane-to-cortex interactions leading to PIP2 release, PIP3 generation, and Rac activation at the opposite side of the cell. We develop a minimal unifying mechanochemical model of the cell to explain how this long-range mechanical facilitation complements local biochemical inhibition to enable robust global Rho and Rac partitioning. Finally, we validate the importance of this long-range facilitation in the context of chemoattractant-based cell polarization and migration in primary human lymphocytes. Our findings demonstrate that the actin cortex and plasma membrane function as an integrated mechanochemical system for long-range partitioning of Rac and Rho during cell migration and likely other cellular contexts.**

**Correspondence:** ***Orion.Weiner@ucsf.edu, herve.turlier@college-de-france.fr***

## Introduction

For proper physiology, many cells need to polarize, or restrict different signaling programs to different portions of their cell surface. Rac and Rho GTPases are key regulators of cell polarity and spatially pattern the actin cytoskeleton for mitosis, morphogenesis, migration, and development (1). Rac is localized to the front migrating cells, where it promotes the extension of sheet-like lamellipodia or pressure-driven blebs **(Figure 1A)** (2, 3). Rho is localized to the back of migrating cells, where it promotes local myosin-2-based contractions and long-range cortical flows (1, 4) **(Figure 1A)**.

While we know that Rho and Rac mutually inhibit each other locally (1, 5–7), how they are properly positioned at opposite ends of the cell during migration remains poorly understood. The majority of models of polarity in migration are based on local biochemical interactions (6, 8–15), with a majority of mathematical models of polarity establishment relying in fact on the so-called wave-pinning mechanism (16–19), where a travelling front of active Rho GTPase is pinned by a bath of cytosolic inactive form. Such mechanism relies importantly on the fast diffusion of the inactive form and a hypothesis of fixed total protein amount. However, previous studies have challenged these requirements, demonstrating that a diffusion-based inhibitor or depletion mechanism is not sufficient to explain neutrophil polarization (20–23). In contrast, local inhibition is not sufficient either to explain the long-rang partitioning of active pools of Rho and Rac and to coordinate front and back at the scale of a migrating cell. The requirement for an additional long-range communication had long been suggested (20–23), but direct evidence and molecular mechanism for this link was unknown.

Cell polarity involves long-range cellular information processing and necessitates information flow at the cellular scale. Forces transmitted via the actin cortex and the plasma membrane have emerged as key conduits for this global coordination. In migration, membrane tension guides shape by relaying actin-based protrusive forces at the front to the contraction of the rear; setting up a global competition that enables the establishment of a single dominant front (24–28). Here we investigate whether the membrane and cortex could act as the mechanical conduit for long-range coordination of the front and back polarity programs.

To probe the long-range spatial coordination of Rac and Rho, we take advantage of optogenetic activators of Rac and Rho in initially unpolarized cells. This enables us to precisely and specifically activate either Rac or Rho in a small region of the cell and observe the global response of the other GTPase. By combining optogenetics with manipulation of cell mechanics and mathematical modeling, we find that both the front and back mutually activate each other at a distance, and this occurs using two distinct pathways. The front stimulates the back via membrane tension, whereas the back stimulates the front via cortical remodeling. We demonstrate the physiological relevance of our findings for immune cell migration using primary human T cells. Our results demonstrate that the actin cortex and plasma membrane act as an integrated mechanochemical system to ensure the proper positioning of the front and back polarity programs during cell migration.

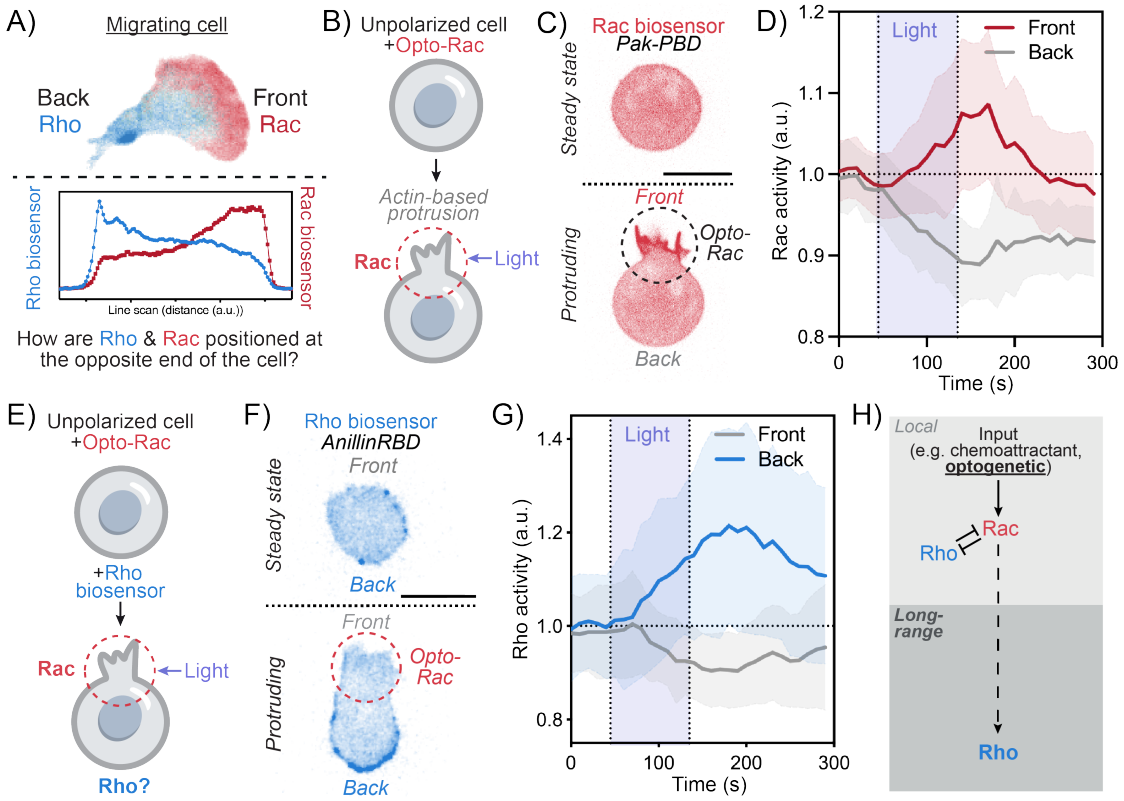


**Fig. 1. Local Rac activation stimulates long-range RhoA activation at the opposite side of the cell.**
(A) Confocal image and associated linescan of a migrating neutrophil-like HL-60 cell expressing the polarity biosensors for Rac (PAK-PBD, in red) and Rho (Anillin-RBD, in blue). In migrating cells, Rac and Rho are localized to the protruding cell front and contracting cell back, respectively. Here we sought to investigate how they appropriately position themselves at the opposite poles of a migrating cell. (B) We locally activated the front polarity program Rac in an initially unpolarized neutrophil-like HL-60 cell using optogenetics (opto-PI3K, see Methods). (C) Time-lapse confocal images of an unpolarized cell before and during opto-Rac stimulation. Rac activity was monitored via the Rac biosensor Pak-PBD. (D) Average time trace of Rac activity at the plasma membrane at the site of opto-Rac activation that becomes the cell front compared to the opposite side of the cell that becomes the cell back. (mean ± SD; n>40, N= 3). (E) We locally activated Rac in an initially unpolarized cell while simultaneously measuring Rho activity using AnillinRBD. (F) Time-lapse confocal images of an unpolarized cell before and during opto-Rac stimulation. Rho activity was monitored using the biosensor AnillinRBD. (G) Average time trace of Rho activity at the plasma membrane at the front and back of the cell following opto-Rac activation. (mean ± SD; n>40, N= 8). (H) Local Rac activation leads to long-range activation of Rho at the opposite side of the cell. Scale bars: 10$\mu$m.

## Results

### Local Rac activation stimulates long-range RhoA activation at the opposite side of the cell.

To investigate how the front and back polarity programs are properly positioned at the opposite ends of the cell, we first analyzed the establishment of cell polarity in a context where we can independently control the spatial and temporal dynamics of each of these programs. Towards this end, we leveraged an optogenetic approach (via local activation of PI3K (29), see Methods), to locally activate the front polarity program Rac in initially unpolarized neutrophil-like HL60 cells **(Figure S1A)**. As previously demonstrated, this local Rac activation leads to actin-driven protrusions like those seen at the cell front during migration **(Figure S1)** (29, 30). Rac activity (visualized with Pak-PBD) is locally enriched in the zone of activation (cell front), while being depleted at the opposite side of the cell (cell back) **(Figure 1B-D, S1B, C and Video S1)**. These results confirm that opto-PI3K locally activates Rac. Next, we sought to investigate how this local zone of Rac activity influences the back polarity program. To this end, we used local Rac activation via opto-PI3K while monitoring the activity of Rho using the biosensor Anillin-RBD **(Figure 1E and Video S2)**. Light-induced Rac activation elicits a rapid long-range increase in Rho activity at the opposite side of the cell **(Figures 1F,G and S1G-I)**. Thus, in addition to locally inhibiting Rho, Rac activation also stimulates Rho at the opposite end of the cell **(Figure 1H)**.

### Rac acts through protrusion-mediated increases in membrane tension for long-range activation of Rho

We next sought to understand how local Rac activation in one part of the cell triggers Rho activity at the opposite end. We considered two possibilities: distal Rho activation could result from local Rac-based biochemical inhibition (1) or indirect long range mechanical signals. One possible means of long-range Rho activation would be Rac-induced protrusions, which generate a membrane tension increase that propagates across the cell (30) **(Figure 2A, B)**. To distinguish between these possibilities, we impaired Rac-mediated protrusion formation by applying pharmacological inhibitors of actin assembly (latrunculin) or Arp2/3 complex activation (CK666) to opto-PI3K cells **(Figure 2C)**. While these perturbations do not impair our ability to optogenetically activate

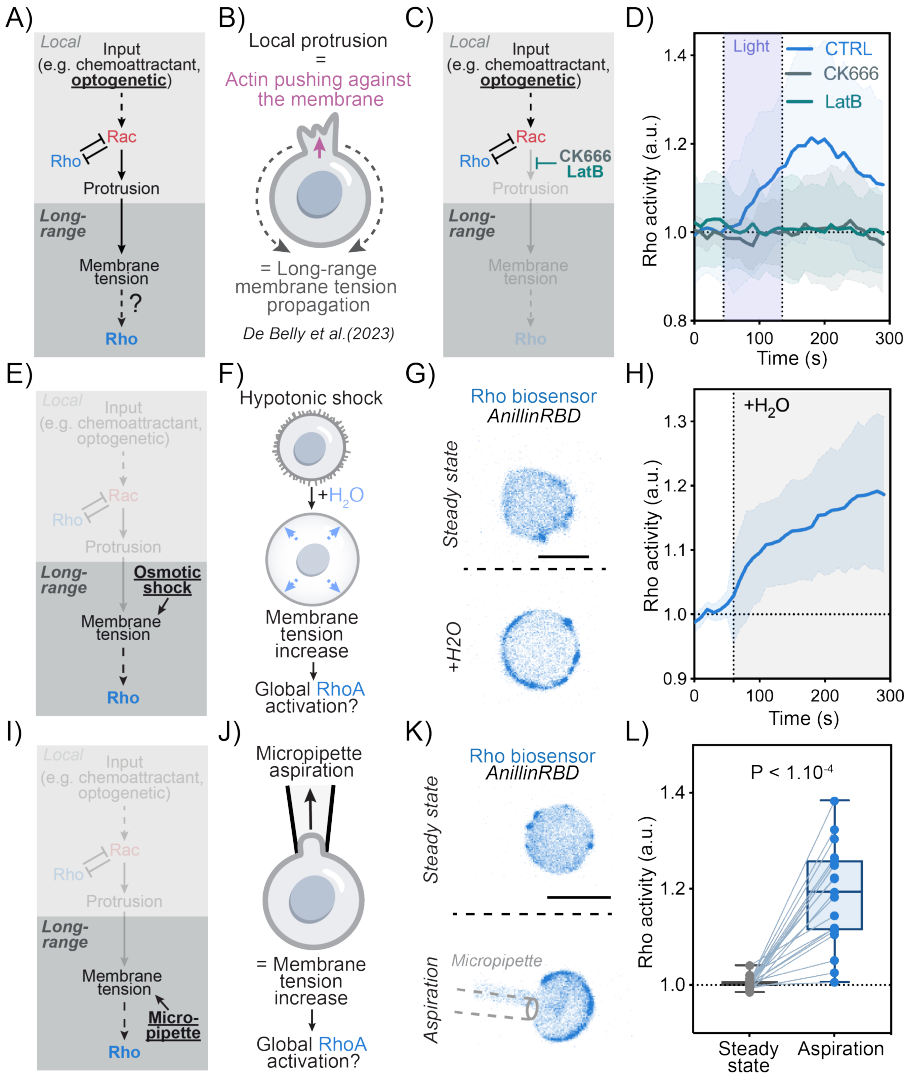


**Fig. 2. Rac acts through protrusion-mediated increases in membrane tension for long-range activation of Rho.**
(A) (B) Local Rac-mediated cell protrusion leads to a global increase in membrane tension. (C) To test the role of protrusions in Rac/Rho crosstalk, we locally activated Rac via optogenetics in the presence of inhibitors of actin assembly (Latrunculin B) or the Arp2/3 complex activation (CK666). (D) Average time trace of Rho activity at the plasma membrane at the back of cells treated with either 10 $\mu$M of Latrunculin B (teal curve) or 100 $\mu$M of CK666 (green curve) demonstrate minimal change in Rho activity following opto-Rac activation (mean ± SD; n>30, N= 3) in contrast to control cells in which the cytoskeleton was not inhibited (same curve as in Fig. 1D). (E) (F) If protrusions activate Rho by elevating membrane tension, then increasing membrane tension (even in the absence of Rac activation) should suffice to activate Rho. Towards this end, we used hypotonic shock to elevate membrane tension. (G) Time-lapse confocal images of an unpolarized opto-Rac HL-60 cell expressing the Rho biosensor (AnillinRBD) before and after hypotonic shock. (H) Average time trace of Rho activity at the plasma before and after hypo-osmotic shock (60 mOsm). Hypotonic-shock-based elevation of membrane tension suffices to globally increase RhoA activity (mean SD; n>30, N= 3). (I) (J) As an alternate approach to increase membrane tension, we leveraged micropipette aspiration. (K) Time-lapse confocal images of an unpolarized opto-Rac HL-60 cell expressing the Rho biosensor (AnillinRBD) before and after micropipette aspiration (see Methods). (L) Average Rho activity before (steady state) and during aspiration. Micropipette-based elevation of membrane tension significantly stimulates Rho activation. Box and whiskers: median and min to max; p values from Wilcoxon paired Student's t test. Scale bars: 10$\mu$m.

Rac (29), they inhibited Rac-mediated Rho activation at the other end of the cell **(Figures 2D and S2A-C)**. Our results support long-range activation of Rho by Rac, operating independently from the well-established local antagonism between these GTPases.

If protrusions stimulate Rho activation through an increase in membrane tension, membrane tension increases should suffice to stimulate Rho activation even in the absence of Rac activation or protrusions. To investigate this possibility, we used hypotonic shock to stimulate an increase in membrane tension (31) **(Figure 2E, F and Video S3)**. Hypotonic shock induced a rapid and global increase in Rho activity across the cell **(Figures 2G,H and S2D-G)**. To verify that this increase in Rho activity is a function of increased membrane tension and not a secondary consequence of the rebuilding of the actin cortex following hypotonic shock, we combined our hypotonic shock assay with Latruculin B treatment, a combination that potently depolymerizes the actin cortex (30, 31). Under these conditions, osmotic shock still activates Rho, indicating that the actin cytoskeleton is not necessary for

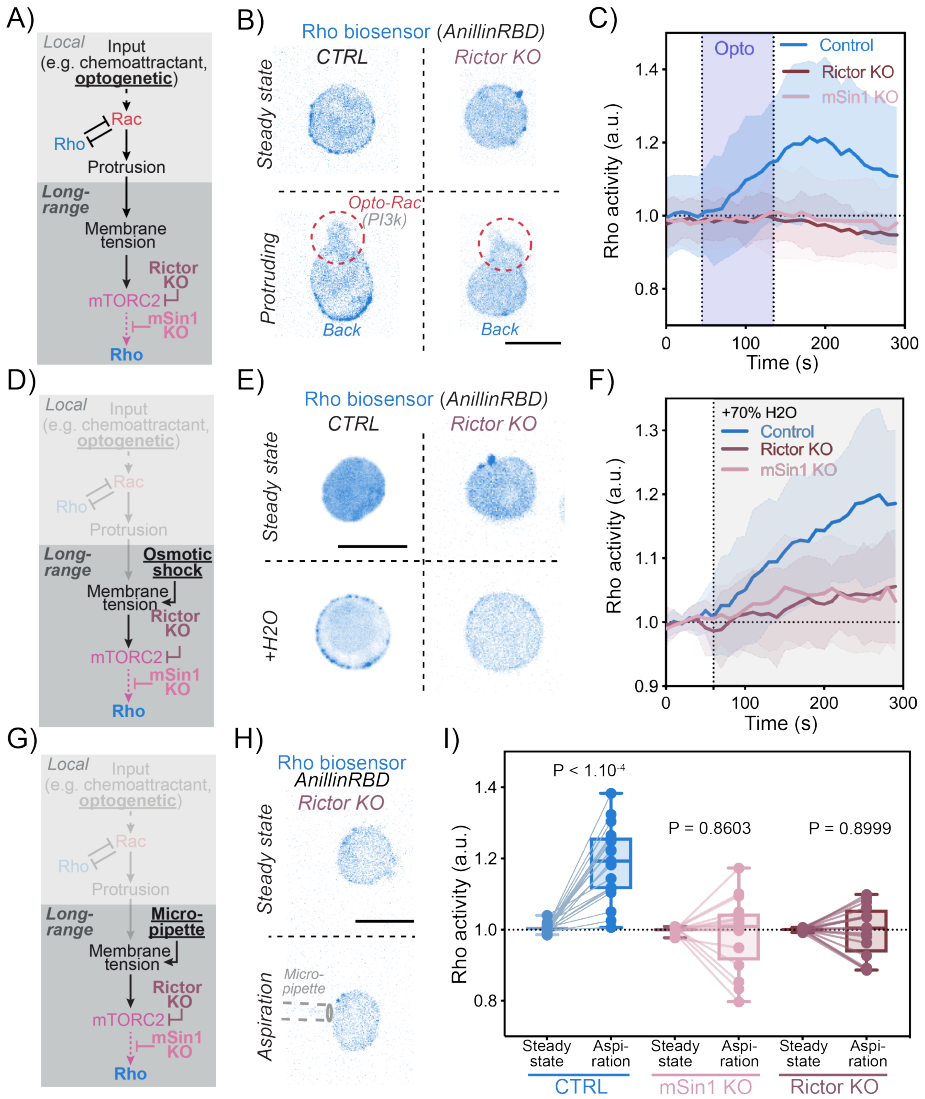


**Fig. 3. mTORC2 links membrane tension increases to Rho activation**
(A) Here we investigated whether mTORC2 is part of the mechanosensory pathway that links increased in membrane tension to the activation of Rho. (B) We used optogenetics to locally activate Rac in control cells versus cells lacking different core components of the mTORC2 complex (Rictor or mSIN1 knockouts). (C) Local Rac activation potently stimulates long-range activation of Rho in control cells (blue) but not cells deficient in two different components of the mTORC2 complex– Rictor KO (magenta) or mSIN1 KO (pink curve), (mean ± SD; n>20, N= 3). Control curve is same as in Fig. 1D. (D) Same as (A) but using hypo-osmotic shock to stimulate membrane tension increase instead of leveraging optogenetically-induced protrusions. (E) Time-lapse confocal images of an unpolarized opto-Rac HL-60 (control) and Rictor KO cell expressing the Rho biosensor (AnillinRBD) before and after hypotonic shock (through 70 percent H20 addition). (F) Average time trace of Rho activity at the plasma membrane before and after hypo-osmotic shock in control, Rictor KO and mSIN1 KO cells demonstrate a requirement for mTORC2 in membrane-tension mediated activation of RhoA (mean ± SD; n>35, N= 3). (G) Same as (A) and (D) but using micropipette aspiration to mechanically stimulate an increase in membrane tension. (H) Time-lapse confocal images of an unpolarized opto-Rac HL-60 Rictor KO cell expressing the Rho biosensor (AnillinRBD) before and after micropipette aspiration. (I) Average Rho activity before (steady state) and during aspiration of control, Rictor KO and mSIN1 KO cells. Values for control are the same as Fig. 2L. Box and whiskers: median and min to max; p values from Wilcoxon paired Student's t test. Scale bars: 10$\mu$m.

membrane-stretch-based Rho activation **(Figure S2H)**. As an alternate approach, we next used a micropipette-based aspiration assay, which we previously demonstrated to increased membrane tension (30). This mechanical manipulation also simulates global Rho activation **(Figures 2I-L and S2I,J and Video S4)**. The activation of Rho by hypotonic shock, micropipette aspiration and opto-induced protrusions likely reflects a role for membrane tension as a Rho activator. Our data show that Rac acts through protrusion-mediated increases in membrane tension to stimulate Rho at a distance.

## mTORC2 links membrane tension increases to Rho activation

Next, we sought to identify the mechanosensors that link increases in membrane tension to Rho activation. The mTORC2 complex emerged as a strong candidate, given its responsiveness to membrane tension and its key roles in regulating cell polarity and motility (26, 27, 31–33). To test whether mTORC2 links membrane tension increases to Rho activation, we performed our opto-Rac activation assay in cells lacking different core components of the mTORC2 complex (Rictor or mSIN1 CRISPR KO cell

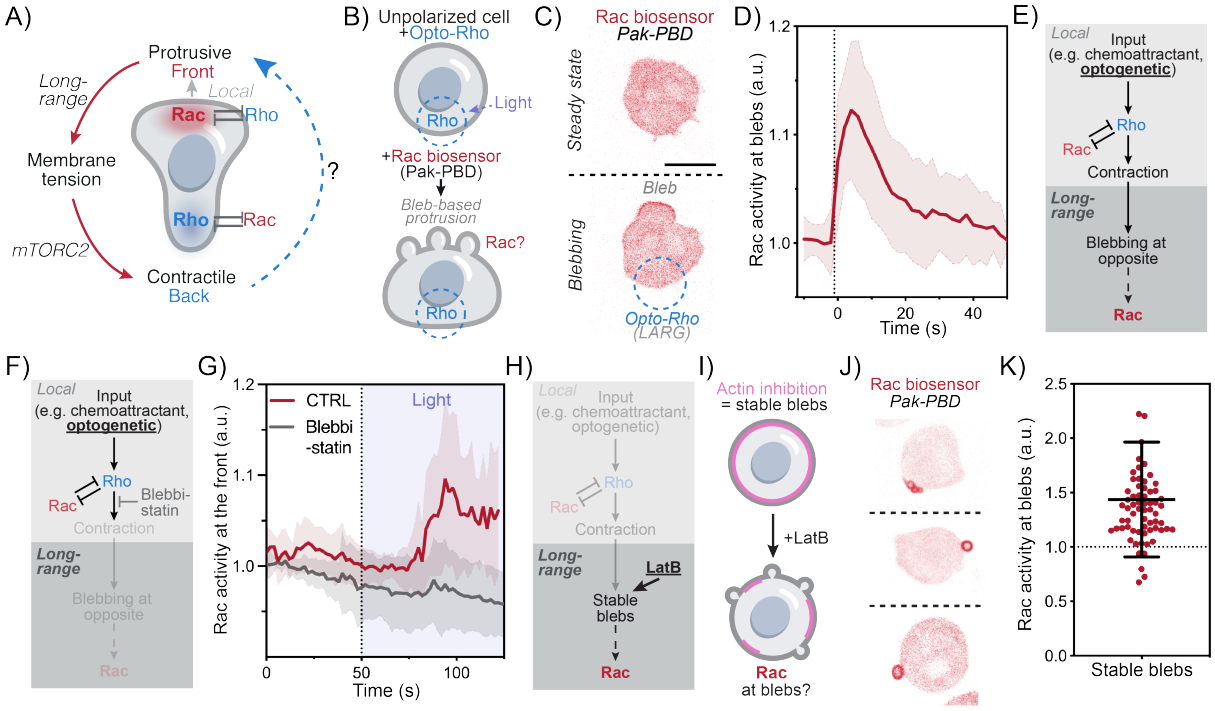


**Fig. 4. Local Rho activation elicits Rac activation at the opposite side of the cell**
(A) The protrusive front activates the back of the cell at a distance via membrane tension. Does the contractile back also activate the front at a distance? (B) We used optogenetics to locally stimulate Rho (opto-LARG, see Methods) while simultaneously measuring Rac activity using the biosensor Pak-PBD. (C) Time-lapse confocal images of an unpolarized opto-Rac HL-60 cell expressing the Rac biosensor (Pak-PBD) before and during opto-Rho stimulation. Local Rho activation induces blebs at the opposite end of the cell, and these blebs are enriched in active Rac. (D) Average time trace of Rac activity at the plasma membrane at the protrusive blebs, which are generated at the opposite end of the cell from opto-Rho. Time 0 = blebbing . For times before blebbing, Rac activity is measured at the same membrane spot where the bleb will appear. (see Methods) (mean ± SD; n > 30, N = 3). (E) We hypothesized that Rho's long-range stimulation of Rac might depend on Rho-based activation of blebbing. (F) We locally activated Rho using optogenetics in the absence or presence of an inhibitor of myosin activation and blebbing (10$\mu$M Blebbistatin). (G) Average time trace of Rac activity at the plasma membrane measured at sites of first bleb appearance (roughly opposite of Opto-Rho, see Figure S4B) in control or cells treated with 10$\mu$M Blebbistatin. This indicates that myosin-based blebbing is important for Rho-mediated activation of Rac activity (mean ± SD; n>20, N= 3). (H) (I) To determine whether blebs suffice for Rac activation in a context independent of Rho-mediated stimulation of actomyosin contractility, we used the actin inhibitor Latrunculin B to generate stable blebs. (J) Three representative confocal images of cells expressing the Rac biosensor Pak-PBD treated with 10 ±M of Latrunculin B demonstrate Rac enrichment in stable blebs. (K) Quantitation of Rac activity in LatrunculinB-induced stable blebs (see Methods) (mean ± SD; n>70, N= 3). Scale bars: 10$\mu$m.

lines) (27) or using a pharmacological inhibition of mTOR **(Figure 3A)**. Cells deficient in mTORC2 (Rictor or mSIN1 KO) or treated with mTOR inhibitor KU-0063794 failed to activate Rho activity upon local Rac-activation **(Figures 3B,C; S3A-E and Video S5)** despite retaining their ability to generate protrusions. To further isolate the tension-mediated potentiation of Rho activity, we repeated previous hypotonic and micropipette aspiration assays in mTORC2-impaired cells. Our results confirmed that mTORC2 is essential for Rho activation following both hypotonic shock **(Figures 3F and S3F,G)** and micropipette aspiration **(Figures 3G-I and S3H-J)**. Our work reveals a molecular pathway in which Rac-induced actin protrusions globally increase membrane tension, activating the mechanosensitive mTORC2, which in turn stimulates Rho.

## Local Rho activation leads to Rac activation at the opposite side of the cell

After establishing that Rac can stimulate Rho activation at a distance, we wondered if the reverse could also be true **(Figure 4A)**. To investigate this, we used an optogenetic approach to locally activate the back polarity program Rho (via LARG, see Methods) while simultaneously monitoring Rac activity using the biosensor Pak-PBD **(Figure 4B and Video S6)**. Our results show that Rho activation leads to long-range Rac activation at the opposite end of the cell, coinciding with another morphological change— blebbing **(Figure 4C, D)**. Given previous studies linking blebbing to Rac activation (34, 35), we hypothesized that Rho's long-range stimulation of Rac might depend on Rho-induced blebbing **(Figures 4E and S4A-F)**. To test this hypothesis, we used the actomyosin inhibitor blebbistatin to block cellular contraction and blebbing following optogenetic Rho activation **(Figure 4F)**. Indeed, when blebbing was inhibited, Rho could no longer activate Rac at a distance **(Figures 4G and S4G,H)**. Just as Rac requires its downstream cytoskeletal effects (actin polymerization and protrusion generation) to activate Rho at a distance **(Figure 2D)**, Rho relies on its downstream cytoskeletal impact (myosin-based contraction and blebbing) to activate Rac at a distance. To further explore whether blebs suffice to activate Rac independent of Rho-mediated stimulation of actomyosin contractility, we used the actin inhibitor Latrunculin B to induce stable blebs (30) **(Figure 4H, I)**. These stable blebs showed robust Rac enrichment **(Figure 4J, K)**.

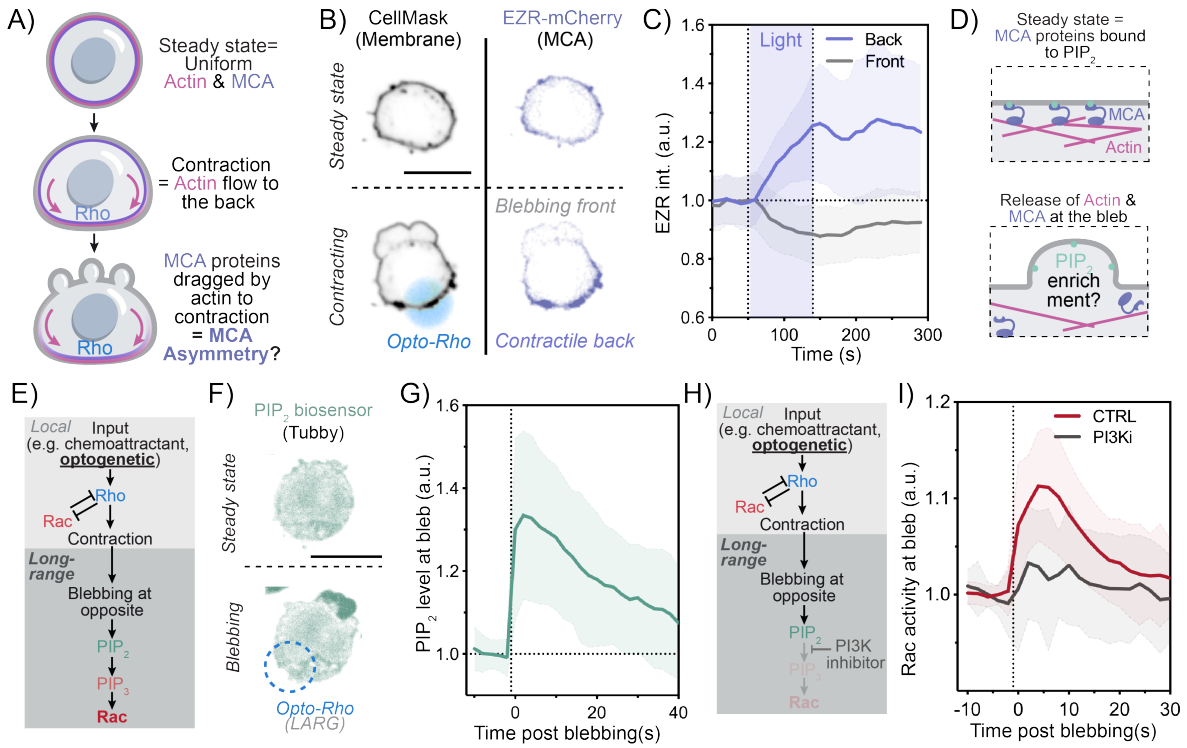


**Fig. 5. Contraction-induced blebbing leads to PIP2 release and PI3K-dependent Rac activation at the opposite side of the cell**
(A) In unpolarized cells at steady state, actin and MCA proteins are uniformly distributed. Upon local contraction (for example induced by opto-Rho), Actin flows toward the site of contraction. We ask whether MCA also flow with the cytoskeleton toward the site of contraction to induce an MCA asymmetry across the cell. (B) Time-lapse confocal images of unpolarized cells expressing the MCA protein Ezrin-mCherry and stained with the membrane marker CellMask before and during opto-Rho stimulation. (C) Average time trace of relative Ezrin intensity at the back (purple) and front (grey) of the cell in response to opto-Rho activation (at the back). (N = 3, n >40, means ± SD). (D) Local Rho-induced contractions lead to MCA flow toward the site of contraction and depletion of MCA at the opposite end of the cell, resulting in blebbing at the cell pole away from opto-Rho. (E) We hypothesized that MCA detachment from plasma membrane during blebbing leads to PIP2 release. (F) Time-lapse confocal images of an unpolarized opto-Rac HL-60 cell expressing the PIP2 biosensor (Tubby) before and during opto-Rho stimulation demonstrates PIP2 enrichment in bleb-based protrusions. (G) Average time trace of PIP2 accumulation at the protrusive blebs (opposite side of the cell from Rho activation) (mean ± SD; n>30, N= 3). (H) Model of Rac activation in protrusive blebs in which detachment of MCA from plasma membrane during blebbing leads to PIP2 release from MCA. PIP2 acts as a substrate for PI3K to generate the Rac activator PIP3. (I) Average time trace of Rac activity at the plasma membrane at the protrusive blebs in control and cells treated with 1 $\mu$M PI3Kδ/γ inhibitor, Duvelisib demonstrates a requirement for PI3K for Rac activation in protrusive blebs (mean ± SD; n>30, N= 3). Control data is the same as in Figure 4D. Scale bars: 10$\mu$m.

Our data demonstrate that local Rho activation stimulates Rac activity at the opposite end of the cell through actomyosin-based blebbing.

**Contraction-induced membrane-to-cortex attachment asymmetry leads to PIP2 release and PI3K-dependent Rac activation at the opposite side of the cell**

We found that Rac is recruited to blebs opposite the contractile back of the cell, but what determines the position of these blebs relative to the Rho-mediated contraction site? Blebs form when the plasma membrane detaches from the underlying actin cortex, and this process is facilitated by a low local concentration of membrane-to-cortex attachment (MCA) proteins. Localized contraction induces actomyosin flow toward the site of Rho mediated-contraction (30). This flow could cause MCA proteins to accumulate at the site of contraction while depleting them from the opposite end of the cell (36–38) **(Figure 5A)**. To test this hypothesis, we imaged cells expressing a fluorescent tagged ezrin, a core MCA protein in neutrophils. Upon local Rho activation, ezrin accumulated at the site of contraction and was depleted at the opposite side of the cell **(Figure 5B-D, S5A-C and Video S7)**. To further validate these findings, we used actin-membrane proximity biosensor MPAct (39) to assess MCA distribution during opto-contraction. This tool confirmed that local contraction enriches MCA at the contraction site while depleting it from the opposite side of the cell **(Figure S5D-F)**. These results suggest that the depletion of MCA opposite to the contraction site promotes the formation of bleb-based sites of Rac activation.

We next explored the molecular mechanism linking blebbing to Rac activation, hypothesizing the lipid composition of the blebs to play a critical role. Because MCA proteins such as ERMs (Ezrin, Radixin, Moesin) bind to the membrane through interactions with PIP2 (40), detachment of MCA proteins from the membrane during blebbing could increase the local concentration of accessible PIP2 **(Figure 5E)**. PI3K could act on this newly-released PIP2 to produce PIP3, a known activator of Rac. To test this hypothesis, we used the PIP2 biosensor Tubby (41) in conjunction with local opto-Rho activation and observed a marked increase in PIP2 level at blebs induced by Rho mediated contraction **(Figure**

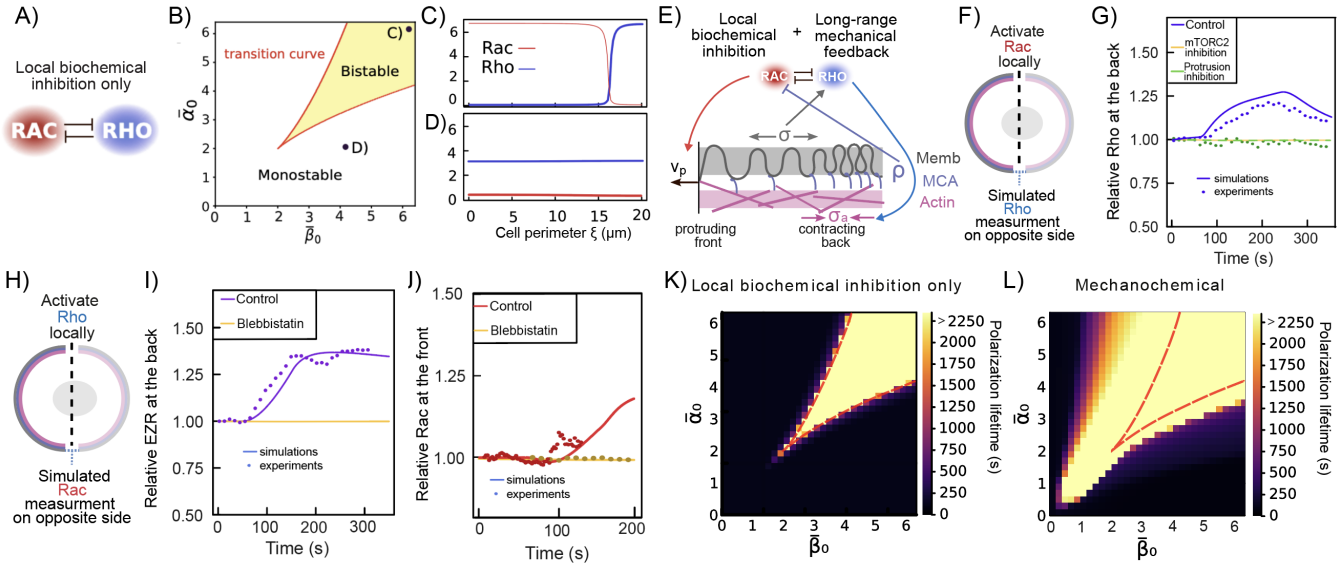


**Fig. 6. Modelling Rac and Rho polarization mechanisms through local inhibition and long-range mechanical feedback**
(A) Simple model of local inhibition between Rac and Rho (B) Phase diagram of polarity obtained from stability analysis using a simple model of local mutual inhibition between Rac and Rho. For any given Rac and Rho basal levels ($\alpha$ and ß respectively), the system is either monostable (unpolarized) or bistable (polarized). (C) (D) Concentration values of Rac and Rho for simulations inside (C) and outside (D) the bistable region, where (C) is polarized with a high value of Rac at the front of the cell and low at the back and vice-versa for Rho. (E) Mechanochemical model of Rac and Rho polarity, combining local mutual inhibition with long-range mechanical feedback. (F) Rac is locally activated on one end (the 'front') of the cell , while Rho activity is measured at the opposite end (the 'back') of the simulated cell. (G) Simulated (solid lines) and experimental (dots) Rho activity at the back of the cell following Rac activation at the front. Control cells are shown in blue, mTORC2 defective cells (Rictor KO) in orange, cells with inhibited protrusions (CK666) in green. (H) Rho is locally activated on one end (the 'back') of the cell , while Rac activity is measured at the opposite end (the 'front') of the simulated cell. (I) Simulated (solid lines) and experimental (dots) Ezrin levels at the back of the cell show that local Rho activity leads to MCA asymmetry. Control is shown in purple while cells with impaired contraction (blebbistatin) are shown in yellow (J) Relative Rac concentration at the front of the cell. The higher discrepancy between model and data here is explained by the fact that Rac activity is dependent on blebbing which varies across cells both in term of timing (Figure S4C) and numbers of blebs per cells (Figure S4D). Here experimental Rac levels are shown only for the first wave of blebbing (Figure S4F). (K) (L) Heatmap of the time needed for a polarized cell to relax back to steady state in function of basal Rac and Rho activity ($\alpha$ and ß respectively) using local inhibition only (K) vs fully integrated mechanochemical model (L).

**5E,F and Video S8)**. Next, we examined the functional role of this PIP3 in Rac activation within blebs by inhibiting PI3K using Duvelisib (PI3Ki), a dual PI3Kδ/γ inhibitor (42) **(Figures 5H and S5G, H)**. Cells treated with Duvelisib displayed a significant impairment Rac enrichment in blebs, both following opto-Rho activation **(Figure 5I)** and in Latrunculin-induced stable blebs **(Figure S5I,J)**. These findings provide a molecular mechanism to link local Rho activation to Rac activation at the opposite end of the cell. Local Rho-induced contraction redistributes MCA proteins away from the opposite end of the cell, promoting blebbing. This depletion of MCA proteins releases PIP2, which serves as a substrate for PI3K to generate the Rac activator PIP3.

**Mechanochemical model of Rho and Rac partitioning in cells.**

Our experiments demonstrate that beyond local mutual inhibition, the front and back polarity programs activate each other over long distances using two distinct mechanisms: membrane tension, which links front generation with back activation, and cortical remodeling, which connects back activation with front generation. To understand the key requirements for this long-range mutual activation, we developed a minimal mechanochemical model of Rho and Rac partitioning. We first formulated a mathematical model using two coupled differential equations to describe the local mutual inhibition between Rac and Rho (43) (**Figure 6A, Supplemental theory**). The model defines two regions of stability for Rac and Rho, depending on their respective levels of antagonism-modulated activation, denoted $\alpha 0$ and ß0. At low or highly asymmetric production levels, only Rho or Rac will dominate (monostable regime), while at sufficiently high levels of both GTPases, a bistable regime arises where they can coexist (**Figure 6B-D**). In the bistable regime, one could force the system locally to be either in a high Rac or Rho state (**Figure 6C**), polarization cannot emerge spontaneously from this simplified biochemical picture only. This highlights the limitations of polarity regulation based only on local inhibition, consistent with our previous experimental results (**Figure 2, 4, S2, S4**).

Next, we combined this mutual local inhibition model with a mechanical model describing the membrane-cortex interplay, building on previous works (30) (see Supplemental theory) (**Figure 6E**). In this model, the cortex is treated as a viscous-contractile layer attached to the membrane via MCA proteins of varying surface density ρ. Membrane tension is generated by entropic forces and cortical-flow-driven ruffles. Rac was assumed to promote protrusion, modeled by a velocity (vp) at the front, while Rho mediated contraction at the back (σa). Based on previous experimental findings, we further introduced two novel couplings: activation of active Rac is negatively modulated by MCA protein density, and

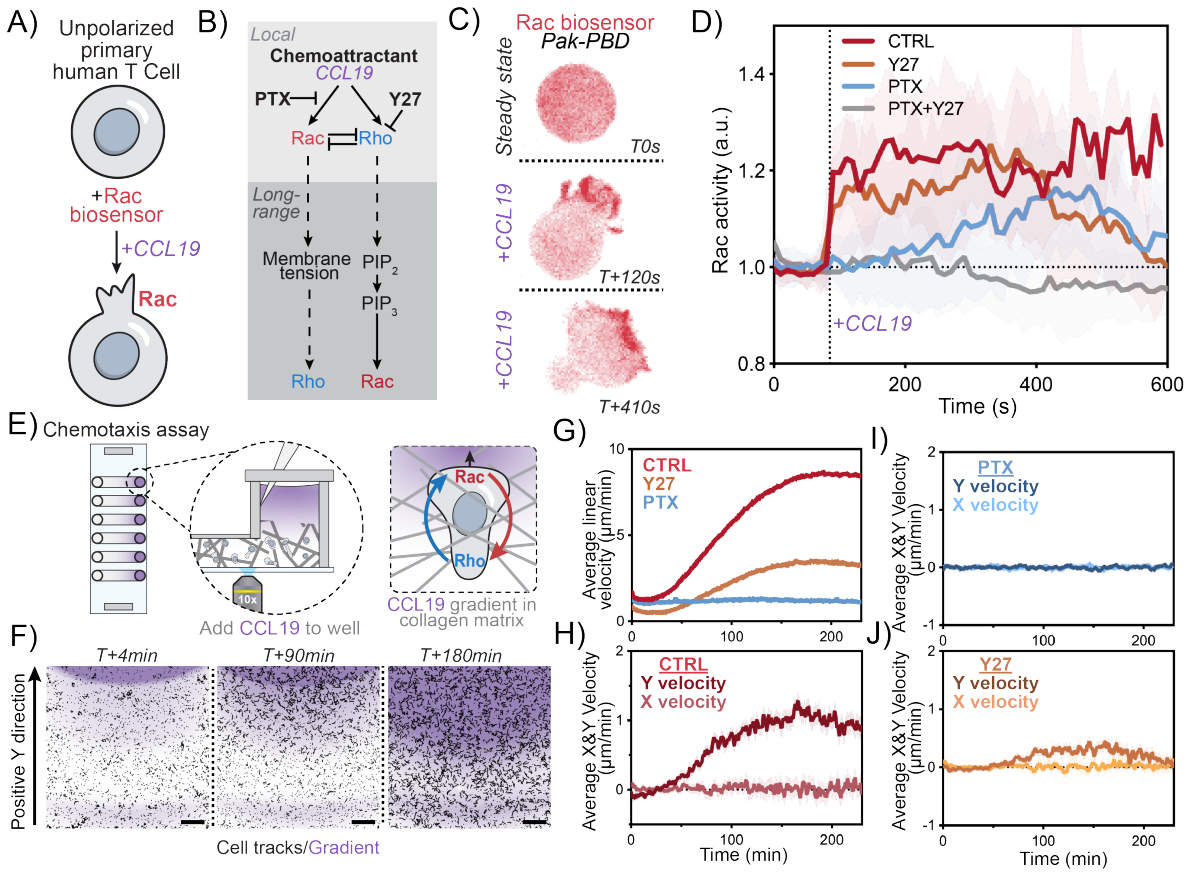


**Fig. 7. Long range mutual activation establishes robust Rho and Rac polarity during primary T cell migration**
(A) Primary human T cells expressing the Rac biosensor (Pak-PBD) to assay cell polarization following acute stimulation with the chemoattractant CCL19. (B) CCL19 is known to activate both Rho and Rac. (C) Time-lapse confocal images of an unpolarized human primary T cell before and during CCL19 stimulation. Rac activity was monitored via the Rac biosensor Pak-PBD. (D) Average time trace of Rac activity at the cell front following addition of 25nM of CCL19 comparing control cells (red), cells treated with 1 $\mu$g/ml of GI inhibitor PTX (blue), cells treated with 20$\mu$M of Y27 (orange) and a combination of PTX and 20$\mu$M Y27 (grey). (mean ± SD; n>20, N = 3 ). (E) Ex-vivo assay for human primary T cell chemotaxis. Cells are premixed with Bovine Dermal Collagen and placed into linear channels. After collagen sets, media is added to one side of the channel (TCM) and media with human CCL19 (100ng total) and 10ug/mL of Dextran10k-AF647 (Dex647) is added to the other. Imaging takes place right on the edge of the well containing CCL19 so that T cell responses can be recorded as the CCL19 (as read out by Dex647) diffuses into the channel. (F) Representative control experiment is shown at different timepoints with Dex647 fluorescence (top row) and corresponding tracks of T cells (bottom row); tracks display 3 minutes preceding timepoint listed. (G) Average linear velocity of all tracks at each timepoint recorded. Control volunteer N = 3, PTX Volunteer N = 3, Y27 Volunteer N = 2. (H)(I)(J) Average Y only component of velocity of all tracks at each timepoint recorded. Positive is considered towards the well containing CCL19. Control Volunteer N = 3, PTX Volunteer N = 3, Y27 Volunteer N = 2.

Rho is enhanced by membrane tension, each governed by switch-like functions. Using this mechanochemical model, we successfully replicated our previous findings showing where local opto-Rac activation resulted in Rho activation at the cell's opposite (**Figure 6F, G**). In line with our experiments, blocking Rac's influence on membrane tension (e.g., via drugs inhibiting protrusion) or disrupting tension's effects on Rho activation (e.g., in mTORC2 mutants) prevented Rac from stimulating Rho activation at the distal end. This integrated mechanochemical model explains how the front positions the back by combining local inhibition and long-range, tension-mediated Rho activation. We next simulated the reverse scenario by locally activating Rho and measuring Rac act the opposite end (**Figure 6H**). The model captured how Rho-driven creates MCA asymmetry (**Figure 6I**) and induces Rac activation at the distal pole (**Figure 6J**). The minor discrepancy between model and data for Rac activation may be due to variability in blebbing across cells, both in timing (**Figure S4C**) and quantity (**Figure S4D**).

Finally, we compared the persistence time of polarity obtained from the integrated mechanochemical model to those generated by a model that includes only local Rac-Rho inhibition. We found that the mechanochemical model allows cells to maintain polarity across a broader range of Rho and Rac production levels (**Figure 6K, L**). Our integrated model suggests that local mutual inhibition alone is insufficient to robustly partition Rho and Rac across the cell. In contrast, combining local mutual inhibition with long-range mutual activation recapitulates our biological observations.

**Long range mutual activation establishes robust Rho and Rac polarity during primary T cell migration** By using optogenetics to locally simulate either the leading-edge regulator (Rac) or the trailing edge regulator (Rho), we

demonstrate that these programs mutually facilitate one another at a distance when either is triggered directly with light. We next sought to investigate Rac/Rho crosstalk in primary immune cells during chemoattractant-based cell polarization and movement. To this end, we used primary human T cells expressing the Rac biosensor (Pak-PBD) to assay cell polarization following acute stimulation with the chemoattractant CCL19, which activates both Rac and Rho pathways (44, 45) **(Figure 7A)**.

We first wondered if Rac partitioning depends on both the known local activation via G$\alpha$i signaling as well as the long-range activation via the Rho/myosin pathway defined in this work **(Figure 7B)**. CCL19 induces rapid cell polarization with sustained Rac activity at the front (Figure 7C, D and Video S9). To focus on the role of Rho/myosin on Rac regulation, we first treated cell with pertussis toxin (PTX) to inactivate G$\alpha$i signaling. These cells maintained their ability to stimulate Rac activation and polarization, albeit with a significant delay and more transiently than control cells **(Figure 7D and S7E, F)**. The ability of PTX treated cells to polarize in response to chemokines has been previously reported but the mechanism by which this is achieved is unknown (6). To test whether this residual Rac regulation occurred through Rho/myosin activation, we treated cells with both PTX and the actomyosin inhibitor Y27632 **(Figure 7D and S7G, H)**. This combination completely abolished even transient Rac polarization, consistent with a long-range back-to-front signaling link that acts in parallel to G$\alpha$i signaling. We tested whether this back-to-front signaling is also dependent on PI3K activation and found Rac polarization to be blocked when using both PTX and the PI3K inhibitor Duvelisib **(Figure S7I, J)**. To test the importance of this long-range Rho to Rac link in the context of G$\alpha$i -based signaling, we treated cells with Y27632 alone, and this elicited a more transient polarization than is seen for control cells **(Figure S7K, L)**. Our results demonstrate how chemoattractant signaling communicates with the front program in two different ways, one direct route via G$\alpha$i and one indirect route via the back-mediated mechanism we define in this work. Both links are required for robust and sustained polarization.

Next, we sought to test how robust polarization established by long-range Rac-Rho communication might affect chemoattractant induced migration in these cells. To stimulate chemotaxis, we embedded T cells in a 3D collagen matrix in a thin channel with CCL19 placed on one side **(Figure 7E)**. As CCL19 freely diffuses into the channel, a chemotactic gradient is established, and control cells rapidly polarize and chemotax up the CCL19 gradient **(Figure 7F-H and Video S10)**. In contrast, cells treated with PTX or Y27 only briefly polarized and failed to robustly migrate toward the CCL19 gradient **(Figure 7G, I-J)**. These results show that dual activation of Rho and Rac by CCL19 is required for persistent polarization, which is in turn necessary for robust chemokinesis and chemotaxis. In contrast, activating just Rho (PTX) or Rac (Y27) only leads to transient, unstable polarization and is insufficient for long-range chemotaxis.

Our results show that long-range mutual activation of front and back is an essential feature of human lymphocyte polarization and motility. Furthermore, we show that activating either the front or back polarity programs without the other only leads to transient polarization. Dual activation is required to support sustained polarization and efficient chemotactic migration.

## Discussion

Our work demonstrates that the well-appreciated mutual short-range inhibition between Rac and Rho is accompanied by an additional mutual long-range facilitation of the front and back polarity programs in migrating cells. The front reinforces the back via membrane tension mediated mTORC2 activation **(Figure 3 and S3)**. The back reinforces the front via cortical remodeling and localized PIP2 release **(Figure 5 and S5)**. Both modes of long-range facilitation are required for sustained and efficient front organization and chemotaxis in primary human lymphocytes **(Figure 7)**. Understanding the partitioning of Rho and Rac in migrating cells has long been a challenge due to the difficulty in establishing the range and directionality of interactions of Rac and Rho. Our use of optogenetics in unpolarized cells enables us to dissect the long-range positive interactions between the front and back programs, and our combined mechanical and biochemical models complement our experimental work by revealing the importance of these links to cell polarization. Our combined multidisciplinary approach is likely to be similarly powerful for other complex interconnected spatiotemporal signaling networks such as axon specification (46), asymmetric cell division (47), epithelial polarity (48), planar cell polarity (49), branching morphogenesis (50), lumen formation (51), and collective cell migration (52).

Robust cell polarization necessitates long-range integration of signals across the cell. A number of currencies have been proposed for this long-range signal relay: diffusion of signals across the cell (14, 17, 43, 53, 54) or force-mediated communication via propagation of forces in the membrane or cortex (24–26, 28, 55) or advection of cellular components via force asymmetries across the cell (56–58) . Membrane tension rapidly propagates across cells and is used for long-range integration of cellular processes from cell spreading (59, 60) to phagocytosis (61) to the competition of fronts that enables a dominant protrusion in migrating cells (25, 26). Tension-based communication is particularly powerful for global signal transmission across the cell(62). Our work shows that membrane tension also enables the front to facilitate contraction at the cell rear through mTORC2 activation. This front-back communication has been suggested in previous studies (6, 20, 21, 56), and our work provides direct evidence for and a molecular mechanism for this link **(Figure 3)**. The evolutionarily-conserved mTORC2 is also the mechanosensitive pathway that enables

competition between fronts(26, 27), regulation of plasma membrane homeostasis in budding yeast (63, 64), and chemotaxis in cells from neutrophils (32) to Dictyostelium (65). Given the evolutionarily conserved role of mTORC2, it would be interesting to probe in future work whether the mTORC2 mediated activation of Rho in response to elevated membrane tension is important in other contexts such as cell division.

Force-mediated flow of components is another powerful mechanism of long-range cell communication (56, 66, 67). Our work shows that flow of MCA components secondary to Rho-mediated actin-based contractions enables the cell rear to establish a Rac-based protrusive front at the opposite end of the cell. These flow-mediated modes of communication are an efficient means for the polarized distribution of signals—in this case the depletion of MCA sites and the facilitation of Rac activation at the opposite end of the cell from Rho-mediated contractions. Flow of cellular signals from the cell front to the cell back along retrograde flows or cortical contractions have been proposed to enable robust polarization (56, 66, 67). Our work provides a molecular mechanism for this long-range integration. It is interesting that the long-range back-to-front and front-to-back communication involve different currencies of membrane tension and cortical flow. These different currencies have different spatial patterns of propagation (relatively global for membrane tension and polarized for cortical flows) and also differ in their molecular requirements, potentially enabling these modes of communication to be independently modulated without interfering with one another.

Rho GTPases are central regulators of the cytoskeleton, and their partitioning underlie many fundamental cellular functions such as cell shape, adhesions and division1. In the context of cell locomotion, we find that long-range activation is a key complement to local inhibition to ensure the proper partitioning of Rac and Rho at opposite poles of the cell. Our findings and model highlight the limitations of a system that relies only on local interactions for spatial segregation. We speculate that the coupling between local biochemical interactions and long-range mechanical facilitation is a conserved feature of Rho GTPases partitioning. This is in good agreement with other systems in which Rho GTPase partitioning relies on long-range communication via the actin and the membrane, from polarization in early C. elegans embryos by cortical flow (68), to axon branching in neuron via long-range membrane tension propagation (46), to the winner-take-all competition enabling a single front during migration (25, 26). Long-range mechanochemical interactions represent a conserved mechanism to complement local biochemical interactions for the partitioning of Rho GTPases in cell migration and likely other processes.

**ACKNOWLEDGEMENTS**

We thank the Weiner and Turlier lab for their critical feedback. We especially want to thank Kate Cavanaugh for kindly sharing the PIP2 biosensor construct and Juan Manuel García-Arcos for his helpful insights. We also thank the blood donors that made the primary human T cell experiment possible. This work was supported by R35GM118167 (ODW, ES), National Science Foundation/Biotechnology and Biological Sciences Research Council grant 2019598 (ODW), K99GM154115 (HDB), the European Research Council (ERC) under the European Union's Horizon 2020 research and innovation program (Grant agreement No. 949267) (HT), the European Union's Horizon 2020 research and innovation program under the Marie Sklodowska-Curie grant agreement No. 101150259 (AFG), the American Heart Association predoctoral fellowship 24PRE1198865 (PJZ) and R21AI1739938 (JKB). HT and AFG are supported by the CNRS and Collège de France.

## Bibliography

1. William M. Bement, Andrew B. Goryachev, Ann L. Miller, and George von Dassow. Patterning of the cell cortex by rho GTPases. pages 1–19. ISSN 1471-0080. doi: 10.1038/s41580-023-00682-z. Publisher: Nature Publishing Group.
2. Juan Manuel García-Arcos, Ankita Jha, Clare M. Waterman, and Matthieu Piel. Blebology: principles of bleb-based migration. 0(0), . ISSN 0962-8924, 1879-3088. doi: 10.1016/j.tcb.2024.02.009. Publisher: Elsevier.
3. Matteo Parri and Paola Chiarugi. Rac and rho GTPases in cancer cell motility control. 8(1): 23. ISSN 1478-811X. doi: 10.1186/1478-811X-8-23.
4. Olivier Pertz, Louis Hodgson, Richard L. Klemke, and Klaus M. Hahn. Spatiotemporal dynamics of RhoA activity in migrating cells. 440(7087):1069–1072. ISSN 1476-4687. doi: 10.1038/nature04665.
5. K. Rottner, A. Hall, and J. V. Small. Interplay between rac and rho in the control of substrate contact dynamics. 9(12):640–648. ISSN 0960-9822. doi: 10.1016/s0960-9822(99)80286-3.
6. Jingsong Xu, Fei Wang, Alexandra Van Keymeulen, Paul Herzmark, Aaron Straight, Kathleen Kelly, Yoh Takuwa, Naotoshi Sugimoto, Timothy Mitchison, and Henry R. Bourne. Divergent signals and cytoskeletal assemblies regulate self-organizing polarity in neutrophils. 114(2):201–214. ISSN 0092-8674. doi: 10.1016/s0092-8674(03)00555-5.
7. M. Hirose, T. Ishizaki, N. Watanabe, M. Uehata, O. Kranenburg, W. H. Moolenaar, F. Matsumura, M. Maekawa, H. Bito, and S. Narumiya. Molecular dissection of the rho-associated protein kinase (p160rock)-regulated neurite remodeling in neuroblastoma n1e-115 cells. 141(7):1625–1636. ISSN 0021-9525. doi: 10.1083/jcb.141.7.1625.
8. Erik Sahai, Raquel Garcia-Medina, Jacques Pouysségur, and Emmanuel Vial. Smurf1 regulates tumor cell plasticity and motility through degradation of RhoA leading to localized inhibition of contractility. 176(1):35–42. ISSN 0021-9525. doi: 10.1083/jcb.200605135.
9. Victoria Sanz-Moreno, Gilles Gadea, Jessica Ahn, Hugh Paterson, Pierfrancesco Marra, Sophie Pinner, Erik Sahai, and Christopher J. Marshall. Rac activation and inactivation control plasticity of tumor cell movement. 135(3):510–523. ISSN 0092-8674. doi: 10.1016/j.cell.2008.09.043.
10. Alfonso Bolado-Carrancio, Oleksii S Rukhlenko, Elena Nikonova, Mikhail A Tsyganov, Anne Wheeler, Amaya Garcia-Munoz, Walter Kolch, Alex von Kriegsheim, and Boris N Kholodenko. Periodic propagating waves coordinate RhoGTPase network dynamics at the leading and trailing edges during cell migration. 9:e58165. ISSN 2050-084X. doi: 10.7554/eLife.58165. Publisher: eLife Sciences Publications, Ltd.
11. Rafael Dominik Fritz and Olivier Pertz. The dynamics of spatio-temporal rho GTPase signaling: formation of signaling patterns. 5:F1000 Faculty Rev–749. ISSN 2046-1402. doi: 10.12688/f1000research.7370.1.
12. Hee Won Yang, Sean R. Collins, and Tobias Meyer. Locally excitable cdc42 signals steer cells during chemotaxis. 18(2):191–201. ISSN 1476-4679. doi: 10.1038/ncb3292. Publisher: Nature Publishing Group.
13. Katrin Martin, Andreas Reimann, Rafael D. Fritz, Hyunryul Ryu, Noo Li Jeon, and Olivier Pertz. Spatio-temporal co-ordination of RhoA, rac1 and cdc42 activation during prototypical edge protrusion and retraction dynamics. 6:21901. ISSN 2045-2322. doi: 10.1038/srep21901.
14. Peter N. Devreotes, Sayak Bhattacharya, Marc Edwards, Pablo A. Iglesias, Thomas Lampert, and Yuchuan Miao. Excitable signal transduction networks in directed cell migration. 33:103–125. ISSN 1530-8995. doi: 10.1146/annurev-cellbio-100616-060739.
15. Yu Deng, Tatsat Banerjee, Dhiman Sankar Pal, Parijat Banerjee, Huiwang Zhan, Jane Borleis, Pablo A. Igleias, and Peter N. Devreotes. PIP5k-ras bistability initiates plasma membrane symmetry breaking to regulate cell polarity and migration. Pages: 2024.09.15.613115 Section: New Results.
16. Alexandra Jilkine, Athanasius F. M. Marée, and Leah Edelstein-Keshet. Mathematical model for spatial segregation of the rho-family GTPases based on inhibitory crosstalk. 69(6):1943–1978. ISSN 0092-8240, 1522-9602. doi: 10.1007/s11538-007-9200-6.
17. Yoichiro Mori, Alexandra Jilkine, and Leah Edelstein-Keshet. Wave-pinning and cell polarity from a bistable reaction-diffusion system. 94(9):3684–3697. ISSN 0006-3495. doi: 10.1529/biophysj.107.120824.
18. Kai H. Kopfer, Willi Jäger, and Franziska Matthäus. A mechanochemical model for rho GTPase mediated cell polarization. 504:110386. ISSN 0022-5193. doi: 10.1016/j.jtbi.2020.110386.
19. Cole Zmurchok, Dhananjay Bhaskar, and Leah Edelstein-Keshet. Coupling mechanical tension and GTPase signaling to generate cell and tissue dynamics. 15(4):046004. ISSN 1478-3975. doi: 10.1088/1478-3975/aab1c0. Publisher: IOP Publishing.
20. Kit Wong, Olivier Pertz, Klaus Hahn, and Henry Bourne. Neutrophil polarization: Spatiotemporal dynamics of RhoA activity support a self-organizing mechanism. 103(10):3639–3644. doi: 10.1073/pnas.0600092103. Publisher: Proceedings of the National Academy of Sciences.
21. Yanqin Wang, Chin-Jen Ku, Elizabeth R. Zhang, Alexander B. Artyukhin, Orion D. Weiner, Lani F. Wu, and Steven J. Altschuler. Identifying network motifs that buffer front-to-back signaling in polarized neutrophils. 3(5):1607–1616. ISSN 2211-1247. doi: 10.1016/j.celrep.2013.04.009.
22. Angela H. Chau, Jessica M. Walter, Jaline Gerardin, Chao Tang, and Wendell A. Lim. Designing synthetic regulatory networks capable of self-organizing cell polarization. 151(2): 320–332. ISSN 0092-8674, 1097-4172. doi: 10.1016/j.cell.2012.08.040. Publisher: Elsevier.

23. Wenzhe Ma, Ala Trusina, Hana El-Samad, Wendell A. Lim, and Chao Tang. Defining network topologies that can achieve biochemical adaptation. 138(4):760–773. ISSN 0092-8674, 1097-4172. doi: 10.1016/j.cell.2009.06.013. Publisher: Elsevier.
24. Jan Mueller, Gregory Szep, Maria Nemethova, Ingrid de Vries, Arnon D. Lieber, Christoph Winkler, Karsten Kruse, J. Victor Small, Christian Schmeiser, Kinneret Keren, Robert Hauschild, and Michael Sixt. Load adaptation of lamellipodial actin networks. 171(1):188–200.e16. ISSN 1097-4172. doi: 10.1016/j.cell.2017.07.051.
25. Andrew R. Houk, Alexandra Jilkine, Cecile O. Mejean, Rostislav Boltyanskiy, Eric R. Dufresne, Sigurd B. Angenent, Steven J. Altschuler, Lani F. Wu, and Orion D. Weiner. Membrane tension maintains cell polarity by confining signals to the leading edge during neutrophil migration. 148(1):175–188. ISSN 0092-8674, 1097-4172. doi: 10.1016/j.cell.2011.10.050.
26. Alba Diz-Muñoz, Kevin Thurley, Sana Chintamen, Steven J. Altschuler, Lani F. Wu, Daniel A. Fletcher, and Orion D. Weiner. Membrane tension acts through PLD2 and mTORC2 to limit actin network assembly during neutrophil migration. 14(6):e1002474. ISSN 1545-7885. doi: 10.1371/journal.pbio.1002474.
27. Suvrajit Saha, Jason P. Town, and Orion D. Weiner. Mechanosensitive mTORC2 independently coordinates leading and trailing edge polarity programs during neutrophil migration. 34(5):ar35. ISSN 1059-1524. doi: 10.1091/mbc.E22-05-0191. Publisher: American Society for Cell Biology (mboc).
28. Arnon D. Lieber, Shlomit Yehudai-Resheff, Erin L. Barnhart, Julie A. Theriot, and Kinneret Keren. Membrane tension in rapidly moving cells is determined by cytoskeletal forces. 23 (15):1409–1417. ISSN 0960-9822. doi: 10.1016/j.cub.2013.05.063.
29. Jason P. Town and Orion D. Weiner. Local negative feedback of rac activity at the leading edge underlies a pilot pseudopod-like program for amoeboid cell guidance. 21(9):e3002307. ISSN 1545-7885. doi: 10.1371/journal.pbio.3002307. Publisher: Public Library of Science.
30. Henry De Belly, Shannon Yan, Hudson Borja da Rocha, Sacha Ichbiah, Jason P. Town, Patrick J. Zager, Dorothy C. Estrada, Kirstin Meyer, Hervé Turlier, Carlos Bustamante, and Orion D. Weiner. Cell protrusions and contractions generate long-range membrane tension propagation. 186(14):3049–3061.e15. ISSN 0092-8674. doi: 10.1016/j.cell.2023.05.014.
31. Chloé Roffay, Guillaume Molinard, Kyoohyun Kim, Marta Urbanska, Virginia Andrade, Victoria Barbarasa, Paulina Nowak, Vincent Mercier, José García-Calvo, Stefan Matile, Robbie Loewith, Arnaud Echard, Jochen Guck, Martin Lenz, and Aurélien Roux. Passive coupling of membrane tension and cell volume during active response of cells to osmosis. 118(47): e2103228118. doi: 10.1073/pnas.2103228118.
32. Lunhua Liu, Satarupa Das, Wolfgang Losert, and Carole A. Parent. mTORC2 regulates neutrophil chemotaxis in a cAMP- and RhoA-dependent fashion. 19(6):845–857. ISSN 1878-1551. doi: 10.1016/j.devcel.2010.11.004.
33. Yuan He, Dong Li, Sara L. Cook, Mee-Sup Yoon, Ashish Kapoor, Christopher V. Rao, Paul J. A. Kenis, Jie Chen, and Fei Wang. Mammalian target of rapamycin and rictor control neutrophil chemotaxis by regulating rac/cdc42 activity and the actin cytoskeleton. 24(21): 3369–3380. ISSN 1059-1524. doi: 10.1091/mbc.E13-07-0405.
34. Meghan K. Driscoll, Erik S. Welf, Andrew Weems, Etai Sapoznik, Felix Zhou, Vasanth S. Murali, Juan Manuel García-Arcos, Minna Roh-Johnson, Matthieu Piel, Kevin M. Dean, Reto Fiolka, and Gaudenz Danuser. Proteolysis-free amoeboid migration of melanoma cells through crowded environments via bleb-driven worrying. ISSN 1534-5807. doi: 10.1016/j.devcel.2024.05.024.
35. Brian R. Graziano, Jason P. Town, Ewa Sitarska, Tamas L. Nagy, Miha Fošnarič, Samo Penič, Aleš Iglič, Veronika Kralj-Iglič, Nir S. Gov, Alba Diz-Muñoz, and Orion D. Weiner. Cell confinement reveals a branched-actin independent circuit for neutrophil polarity. 17(10): e3000457. ISSN 1545-7885. doi: 10.1371/journal.pbio.3000457.
36. Chantal Roubinet, Barbara Decelle, Gaëtan Chicanne, Jonas F. Dorn, Bernard Payrastre, François Payre, and Sébastien Carreno. Molecular networks linked by moesin drive remodeling of the cell cortex during mitosis. 195(1):99–112. ISSN 0021-9525. doi: 10.1083/jcb.201106048.
37. Shota Hiruma, Tomoko Kamasaki, Kohei Otomo, Tomomi Nemoto, and Ryota Uehara. Dynamics and function of ERM proteins during cytokinesis in human cells. 591(20):3296–3309. ISSN 1873-3468. doi: 10.1002/1873-3468.12844. _eprint: https://onlinelibrary.wiley.com/doi/pdf/10.1002/1873-3468.12844.
38. Elgin Korkmazhan and Alexander R. Dunn. The membrane-actin linker ezrin acts as a sliding anchor. 8(31):eabo2779. doi: 10.1126/sciadv.abo2779. Publisher: American Association for the Advancement of Science.
39. Anjali Bisaria, Arnold Hayer, Damien Garbett, Daniel Cohen, and Tobias Meyer. Membrane proximal f-actin restricts local membrane protrusions and directs cell migration. 368(6496): 1205–1210. ISSN 0036-8075. doi: 10.1126/science.aay7794.
40. Andrea I. McClatchey. ERM proteins at a glance. 127(15):3199–3204. ISSN 0021-9533, 1477-9137. doi: 10.1242/jcs.098343.
41. Kathryn V Quinn, Philippe Behe, and Andrew Tinker. Monitoring changes in membrane phosphatidylinositol 4,5-bisphosphate in living cells using a domain from the transcription factor tubby. 586:2855–2871. ISSN 0022-3751. doi: 10.1113/jphysiol.2008.153791.
42. David G. Winkler, Kerrie L. Faia, Jonathan P. DiNitto, Janid A. Ali, Kerry F. White, Erin E. Brophy, Melissa M. Pink, Jennifer L. Proctor, Jennifer Lussier, Christian M. Martin, Jennifer G. Hoyt, Bonnie Tillotson, Erin L. Murphy, Alice R. Lim, Brian D. Thomas, John R. Macdougall, Pingda Ren, Yi Liu, Lian-Sheng Li, Katti A. Jessen, Christian C. Fritz, Joi L. Dunbar, James R. Porter, Christian Rommel, Vito J. Palombella, Paul S. Changelian, and Jeffery L. Kutok. PI3k-δ and PI3k-γ inhibition by IPI-145 abrogates immune responses and suppresses activity in autoimmune and inflammatory disease models. 20(11):1364–1374. ISSN 1879-1301. doi: 10.1016/j.chembiol.2013.09.017.
43. Kate M. Byrne, Naser Monsefi, John C. Dawson, Andrea Degasperi, Jimi-Carlo Bukowski-Wills, Natalia Volinsky, Maciej Dobrzyński, Marc R. Birtwistle, Mikhail A. Tsyganov, Anatoly Kiyatkin, Katarzyna Kida, Andrew J. Finch, Neil O. Carragher, Walter Kolch, Lan K. Nguyen, Alex von Kriegsheim, and Boris N. Kholodenko. Bistability in the rac1, PAK, and RhoA signaling network drives actin cytoskeleton dynamics and cell motility switches. 2(1):38–48. ISSN 2405-4712. doi: 10.1016/j.cels.2016.01.003.
44. José Luis Rodríguez-Fernández and Olga Criado-García. The chemokine receptor CCR7 uses distinct signaling modules with biased functionality to regulate dendritic cells. 11. ISSN 1664-3224. doi: 10.3389/fimmu.2020.00528. Publisher: Frontiers.
45. Lorena Riol-Blanco, Noelia Sánchez-Sánchez, Ana Torres, Alberto Tejedor, Shuh Narumiya, Angel L. Corbí, Paloma Sánchez-Mateos, and José Luis Rodríguez-Fernández. The chemokine receptor CCR7 activates in dendritic cells two signaling modules that independently regulate chemotaxis and migratory speed1. 174(7):4070–4080. ISSN 0022-1767. doi: 10.4049/jimmunol.174.7.4070.
46. Zheng Shi, Sarah Innes-Gold, and Adam E. Cohen. Membrane tension propagation couples axon growth and collateral branching.
47. Bharath Sunchu and Clemens Cabernard. Principles and mechanisms of asymmetric cell division. 147(13):dev167650. ISSN 0950-1991. doi: 10.1242/dev.167650.
48. Clare E. Buckley and Daniel St Johnston. Apical–basal polarity and the control of epithelial form and function. 23(8):559–577. ISSN 1471-0080. doi: 10.1038/s41580-022-00465-y. Publisher: Nature Publishing Group.
49. Mitchell T. Butler and John B. Wallingford. Planar cell polarity in development and disease. 18(6):375–388. ISSN 1471-0080. doi: 10.1038/nrm.2017.11. Publisher: Nature Publishing Group.
50. Tsuyoshi Hirashima and Michiyuki Matsuda. ERK-mediated curvature feedback regulates branching morphogenesis in lung epithelial tissue. 34(4):683–696.e6. ISSN 0960-9822. doi: 10.1016/j.cub.2023.12.049. Publisher: Elsevier.
51. Dhiraj Indana, Andrei Zakharov, Youngbin Lim, Alexander R. Dunn, Nidhi Bhutani, Vivek B. Shenoy, and Ovijit Chaudhuri. Lumen expansion is initially driven by apical actin polymerization followed by osmotic pressure in a human epiblast model. 31(5):640–656.e8. ISSN 1934-5909. doi: 10.1016/j.stem.2024.03.016.
52. Justin Bui, Daniel E. Conway, Rebecca L. Heise, and Seth H. Weinberg. Mechanochemical coupling and junctional forces during collective cell migration. 117(1):170–183. ISSN 0006-3495. doi: 10.1016/j.bpj.2019.05.020.
53. Hans Meinhardt. Orientation of chemotactic cells and growth cones: models and mechanisms. 112(17):2867–2874. ISSN 0021-9533. doi: 10.1242/jcs.112.17.2867.
54. Steven J. Altschuler, Sigurd B. Angenent, Yanqin Wang, and Lani F. Wu. On the spontaneous emergence of cell polarity. 454(7206):886–889. ISSN 1476-4687. doi: 10.1038/nature07119. Publisher: Nature Publishing Group.
55. Juan Manuel García-Arcos, Johannes Ziegler, Silvia Grigolon, Loïc Reymond, Gaurav Shajepal, Cédric J. Cattin, Alexis Lomakin, Daniel J. Müller, Verena Ruprecht, Stefan Wieser, Raphael Voituriez, and Matthieu Piel. Rigidity percolation and active advection synergize in the actomyosin cortex to drive amoeboid cell motility. 0(0), . ISSN 1534-5807. doi: 10.1016/j.devcel.2024.06.023. Publisher: Elsevier.
56. Tony Y.-C. Tsai, Sean R. Collins, Caleb K. Chan, Amalia Hadjitheodorou, Pui-Ying Lam, Sunny S. Lou, Hee Won Yang, Julianne Jorgensen, Felix Ellett, Daniel Irimia, Michael W. Davidson, Robert S. Fischer, Anna Huttenlocher, Tobias Meyer, James E. Ferrell, and Julie A. Theriot. Efficient front-rear coupling in neutrophil chemotaxis by dynamic myosin II localization. 49(2):189–205.e6. ISSN 1878-1551. doi: 10.1016/j.devcel.2019.03.025.
57. Kotryna Vaidžiulytė, Anne-Sophie Macé, Aude Battistella, William Beng, Kristine Schauer, and Mathieu Coppey. Persistent cell migration emerges from a coupling between protrusion dynamics and polarized trafficking. 11:e69229. ISSN 2050-084X. doi: 10.7554/eLife.69229. Publisher: eLife Sciences Publications, Ltd.
58. Xiaoguang Li, Dhiman Sankar Pal, Debojyoti Biswas, Pablo A. Iglesias, and Peter N. Devreotes. Reverse fountain flow of phosphatidylinositol-3,4-bisphosphate polarizes migrating cells. 40(4):e105094. ISSN 1460-2075. doi: 10.15252/embj.2020105094.
59. Drazen Raucher and Michael P. Sheetz. Cell spreading and lamellipodial extension rate is regulated by membrane tension. 148(1):127–136. ISSN 0021-9525, 1540-8140. doi: 10.1083/jcb.148.1.127.
60. Nils C. Gauthier, Marc Antoine Fardin, Pere Roca-Cusachs, and Michael P. Sheetz. Temporary increase in plasma membrane tension coordinates the activation of exocytosis and contraction during cell spreading. 108(35):14467–14472. ISSN 0027-8424. doi: 10.1073/pnas.1105845108.
61. Thomas A. Masters, Bruno Pontes, Virgile Viasnoff, You Li, and Nils C. Gauthier. Plasma membrane tension orchestrates membrane trafficking, cytoskeletal remodeling, and biochemical signaling during phagocytosis. 110(29):11875–11880. ISSN 1091-6490. doi: 10.1073/pnas.1301766110.
62. Henry De Belly and Orion D. Weiner. Follow the flow: Actin and membrane act as an integrated system to globally coordinate cell shape and movement. 89:102392. ISSN 0955-0674. doi: 10.1016/j.ceb.2024.102392.
63. Brad J. Niles, Huzefa Mogri, Andrew Hill, Ariadne Vlahakis, and Ted Powers. Plasma membrane recruitment and activation of the AGC kinase ypk1 is mediated by target of rapamycin complex 2 (TORC2) and its effector proteins slm1 and slm2. 109(5):1536–1541. doi: 10.1073/pnas.1117563109. Publisher: Proceedings of the National Academy of Sciences.
64. Margot Riggi, Beata Kusmider, and Robbie Loewith. The flipside of the TOR coin – TORC2 and plasma membrane homeostasis at a glance. 133(9):jcs242040. ISSN 0021-9533. doi: 10.1242/jcs.242040.
65. Yoichiro Kamimura, Yuan Xiong, Pablo A. Iglesias, Oliver Hoeller, Parvin Bolourani, and Peter N. Devreotes. PIP3-independent activation of TorC2 and PKB at the cell's leading edge mediates chemotaxis. 18(14):1034–1043. ISSN 0960-9822. doi: 10.1016/j.cub.2008.06.068. Publisher: Elsevier.
66. Paolo Maiuri, Jean-François Rupprecht, Stefan Wieser, Verena Ruprecht, Olivier Bénichou, Nicolas Carpi, Mathieu Coppey, Simon De Beco, Nir Gov, Carl-Philipp Heisenberg, Carolina Lage Crespo, Franziska Lautenschlaeger, Maël Le Berre, Ana-Maria Lennon-Dumenil, Matthew Raab, Hawa-Racine Thiam, Matthieu Piel, Michael Sixt, and Raphaël Voituriez. Actin flows mediate a universal coupling between cell speed and cell persistence. 161(2): 374–386. ISSN 1097-4172. doi: 10.1016/j.cell.2015.01.056.
67. Lawrence Yolland, Mubarik Burki, Stefania Marcotti, Andrei Luchici, Fiona N. Kenny, John Robert Davis, Eduardo Serna-Morales, Jan Müller, Michael Sixt, Andrew Davidson, Will Wood, Linus J. Schumacher, Robert G. Endres, Mark Miodownik, and Brian M. Stramer. Persistent and polarized global actin flow is essential for directionality during cell migration. 21(11):1370–1381. ISSN 1476-4679. doi: 10.1038/s41556-019-0411-5.
68. Edwin Munro, Jeremy Nance, and James R. Priess. Cortical flows powered by asymmetrical contraction transport PAR proteins to establish and maintain anterior-posterior polarity in the

**Supplementary figure and videos legends:**

**Video S1**
Time-lapse confocal images of HL-60 cells expressing opto-PI3k (Opto-Rac) and Rac biosensor (Pak-PBD) showing localized Rac activation upon light activation. Related to **Figure 1C, D**. Scale bar: 10um.

**Video S2**
Time-lapse confocal images of HL-60 cells expressing opto-PI3k (Opto-Rac) and Rho biosensor (AnillinRBD) showing that light-induced Rac activation elicits a rapid long-range increase in Rho activity at the opposite side of the cell. Related to **Figure 1F, G**. Scale bar: 10um.

**Video S3**
Time-lapse confocal images of HL-60 cells expressing Rho biosensor (AnillinRBD) before and during osmotic shock performed by directly adding water to the imaging media (70% final). This shows that Rho activity increase in response to increasing membrane tension by osmotic shock. Related to **Figure 2G, H**. Scale bar: 10um.

**Video S4**
Time-lapse confocal images of an HL-60 cell expressing Rho biosensor (AnillinRBD) and stained with membrane marker CellMask before and during micropipette aspiration assay, showing that Rho activity increase in response to mechanically increasing membrane tension. Related to **Figure 2K, L**. Scale bar: 10um.

**Video S5**
First video: Time-lapse confocal images of a Rictor KO HL-60 cell expressing opto-PI3k (Opto-Rac) and Rho biosensor (AnillinRBD) showing that light-induced Rac activation elicits no significant increase in Rho activity at the opposite side of the cell. Related to **Figure 3B, C**. Scale bar: 10um.
Second video: Time-lapse confocal images of a Rictor KO HL-60 cell expressing Rho biosensor (AnillinRBD) before and during osmotic shock performed by directly adding water to the imaging media (70% final) showing no significant change in Rho activity in response to osmotic shock. Related to **Figure 3E, F**. Scale bar: 10um.
Third video: Time-lapse confocal images of a Rictor KO HL-60 cells expressing Rho biosensor (AnillinRBD) and stained with membrane marker CellMask before and during micropipette aspiration assay, showing no significant Rho activity increase in response to mechanically increasing membrane tension. Related to **Figure 3H, I**. Scale bar: 10um.

**Video S6**
Time-lapse confocal images of an HL-60 cell expressing opto-LARG (Opto-Rho) and the Rac biosensor (Pak-PBD) showing that Rho activation leads to long-range Rac activation at the opposite end of the cell, coinciding with another morphological change— blebbing. Related to **Figure 4C, D**. Scale bar: 10um.

**Video S7**
Time-lapse confocal images of an HL-60 cell expressing opto-LARG (Opto-Rho) and Ezrin-mCherry showing that upon local Rho activation, ezrin accumulated at the site of contraction and was depleted at the opposite side of the cell Related to **Figure 5B, C**. Scale bar: 10um.

**Video S8**

Time-lapse confocal images of an HL-60 cell expressing opto-LARG (Opto-Rho) and PIP2 biosensor (Tubby-HaloTag) showing that local Rho activation leads to a marked increase in $PIP_2$ level in blebs. Related to **Figure 5F, G**. Scale bar: 10um.

**Video S9**

Time-lapse confocal images of a primary T Cell expressing the Rac biosensor (Pak-PBD) before and after adding 25nM of CCL19. Related to **Figure 7C, D**.

**Video S10**

Ex-vivo assay for human primary T cell chemotaxis. Cells are premixed with Bovine Dermal Collagen and placed into linear channels. After collagen sets, media is added to one side of the channel (TCM) and media with human CCL19 (100ng total) and 10ug/mL of Dextran10k-AF647 (Dex647) is added to the other. Average linear velocity of all tracks at each timepoint is recorded. In order showing control cells, cells treated with Y27 and cells treated with PTX. Related to **Figure 7E-J**.

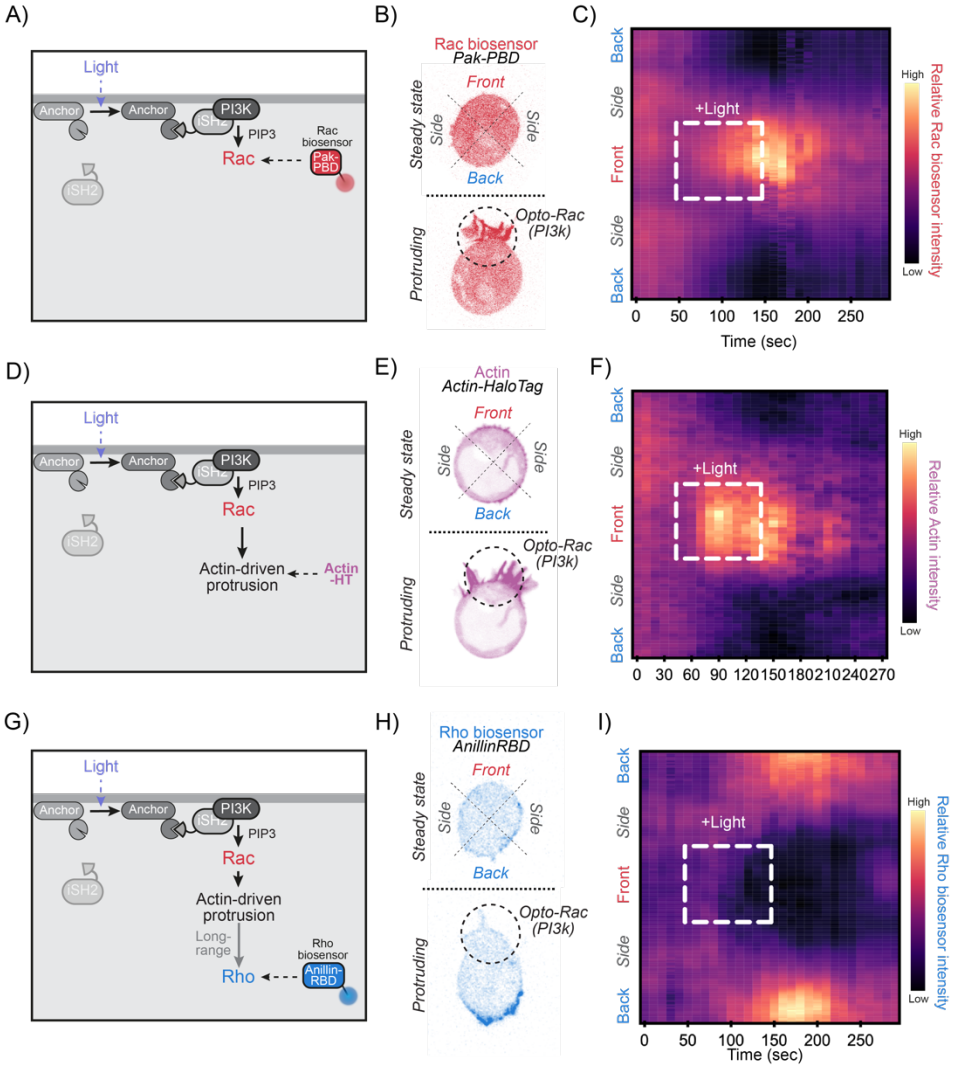


**<u>Figure S1: Optogenetic control of PI3K leads to local Rac activation, which triggers localized actin-driven cell protrusion and long-range Rho activation.</u>**

(A) Schematic of local Rac activation via opto-PI3K. When localized 488-nm light is applied, the membrane anchor protein (iLid-BFP-CAAX) changes conformation, which leads to the binding of inter SH2 domain (iSH2) to the illuminated region. iSH2 then recruits PI3K, whose lipid product ($PIP_3$) induces the activation of Rac GTPase (Rac). We monitor Rac activity using the Rac biosensor Pak-PBD-mCherry, which recognizes and binds the active GTP-bound Rac. (B) Time-lapse confocal images of an unpolarized cell before and during opto-Rac stimulation. Rac activity was monitored via the Rac biosensor Pak-PBD. (C) Kymograph of Rac activity (Pak-PBD intensity) along the normalized cell circumference (y axis) showing that over time (x axis), Rac activity increases at the front in response to opto-PI3K. (N=3, n>40). (D) Rac activation via opto-PI3K leads to localized actin-mediated protrusion, which we monitor by over-expression of Actin-HaloTag. (E) Time-lapse confocal images of an unpolarized cell expressing actin-HaloTag before and during opto-Rac stimulation. (F) Kymograph of actin intensity during opto-PI3k activation (N = 3, n = 25). (G) Long-range Rho activation by local Rac activation is monitored using the Rho Biosensor AnillinRBD, which recognizes the active GTP-bound Rho. (H) Time-lapse confocal images of an unpolarized cell expressing AnillinRBD-mCherry before and during opto-Rac stimulation. (I) Kymograph of Rho activity in response to local Rac activation (opto-PI3k) (N = 8, n > 40).

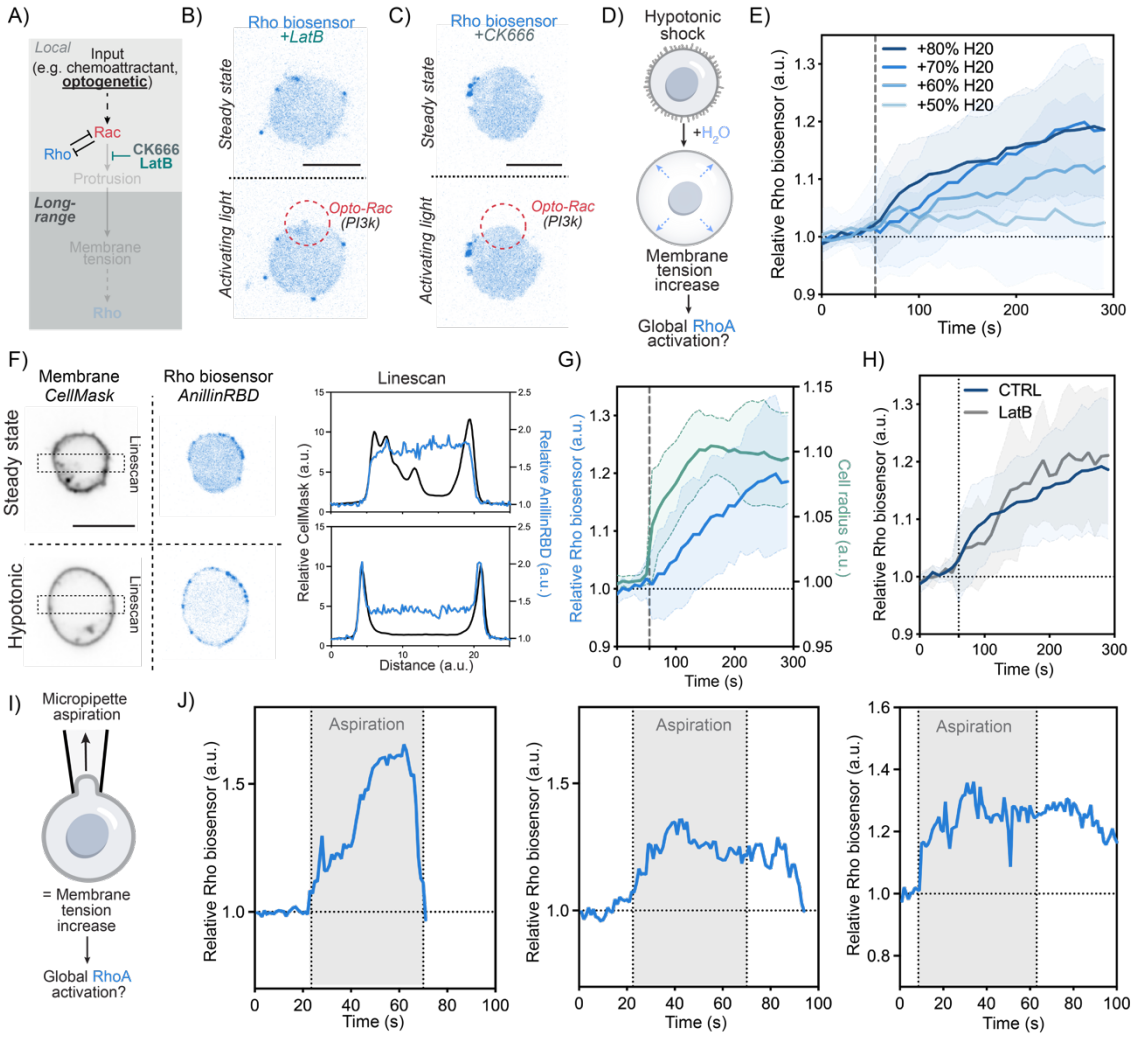


**Figure S2: Rho is activated by increases in membrane tension**

(A) To test the role of protrusions in Rac/Rho crosstalk, we locally activated Rac via optogenetics in the presence of inhibitors of actin assembly (Latrunculin B) or the Arp2/3 complex activation (CK666). (B) (C) Time-lapse confocal images of unpolarized cells expressing AnillinRBD-mCherry before and during opto-Rac stimulation treated with either 10 uM of Latrunculin B (left) or 100 uM of CK666 (right). (D) Osmotic shocks are used to globally increase membrane tension. (E) Average time trace of Rho activity at the plasma membrane in response for hypotonic shocks of various intensity. (N>3, n>20, means ± SD) (F) Left, confocal images of a cell before and during osmotic shock (+70% water) expressing the Rho biosensor AnillinRBD and stained with the plasma membrane marker CellMask. Right, linescan of the Rho and membrane intensity before and during osmotic shock, showing a decrease in background biosensor in the cytoplasm (cytoplasmic dilution) and a recruitment of the biosensor at the plasma membrane. (G) Left y axis, average time trace of Rho activity at the membrane (in blue) in response to hypotonic shock (70% water). Right y axis, cell radius over time (green). (N = 2, n >15, means ± SD) (H) Average time trace of Rho activity at the membrane in response to hypotonic shock (80% water) for control cells (blue) or cells treated with 10 uM of Latrunculin B (grey), showing that actin inhibition doesn't impair Rho recruitment in response to elevated membrane tension. (N = 3, n >30, means ± SD) (I) As an alternate approach to increase membrane tension, we leveraged micropipette aspiration[30] (J) Three example time trace of Rho activity at the plasma membrane in response to micropipette aspiration. Scale bars: 10um.

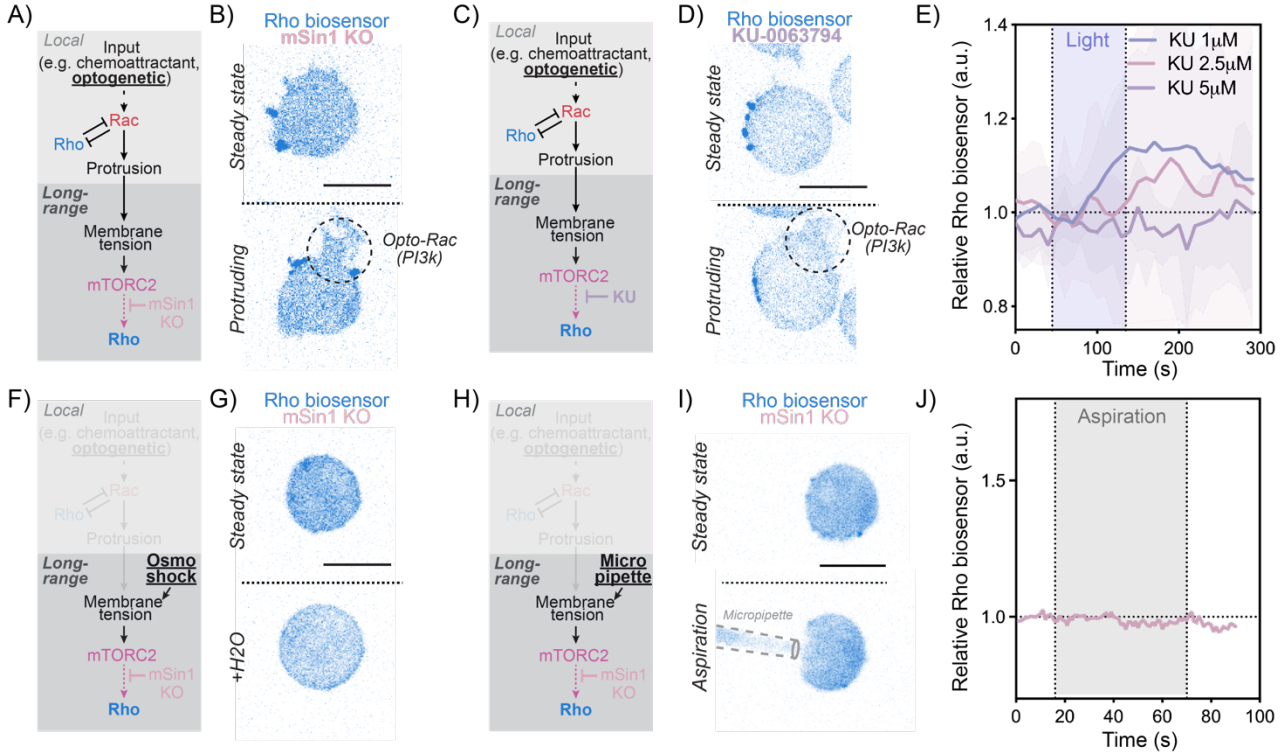


**Figure S3: Impairing mTORC2 prevents tension-mediated Rho activation**

(A) Optogenetics to locally activate Rac in cells lacking core components of the mTORC2 complex (mSIN1 knockouts). (B) Time-lapse confocal images of unpolarized mSIN1 KO cells expressing AnillinRBD-mCherry before and during opto-Rac stimulation. (C) We used the mTOR inhibitor KU-0063794 to prevent Rho activation in response to opto-Rac stimulation. (D) Time-lapse confocal images of unpolarized cells expressing AnillinRBD-mCherry treated with 5uM of KU-0063794 before and during opto-Rac stimulation. (E) Average time trace of Rho activity in opto-Rac cells treated with either 1uM (blue), 2.5uM (pink) or 5uM (purple) of KU-0063794. (N = 2, n > 8). (F) Osmotic shock to globally increase membrane tension in cells lacking core components of the mTORC2 complex (mSIN1 knockouts). (G) Time-lapse confocal images of unpolarized mSIN1 KO cells expressing AnillinRBD-mCherry before and during hypotonic shock (70% Water). (H)(I) Same as (F)(G) but using a micropipette to mechanically increase membrane tension. (J) Example time trace of Rho activity at the membrane of a mSIN1 KO cell during micropipette aspiration assay. Scale bars: 10um.

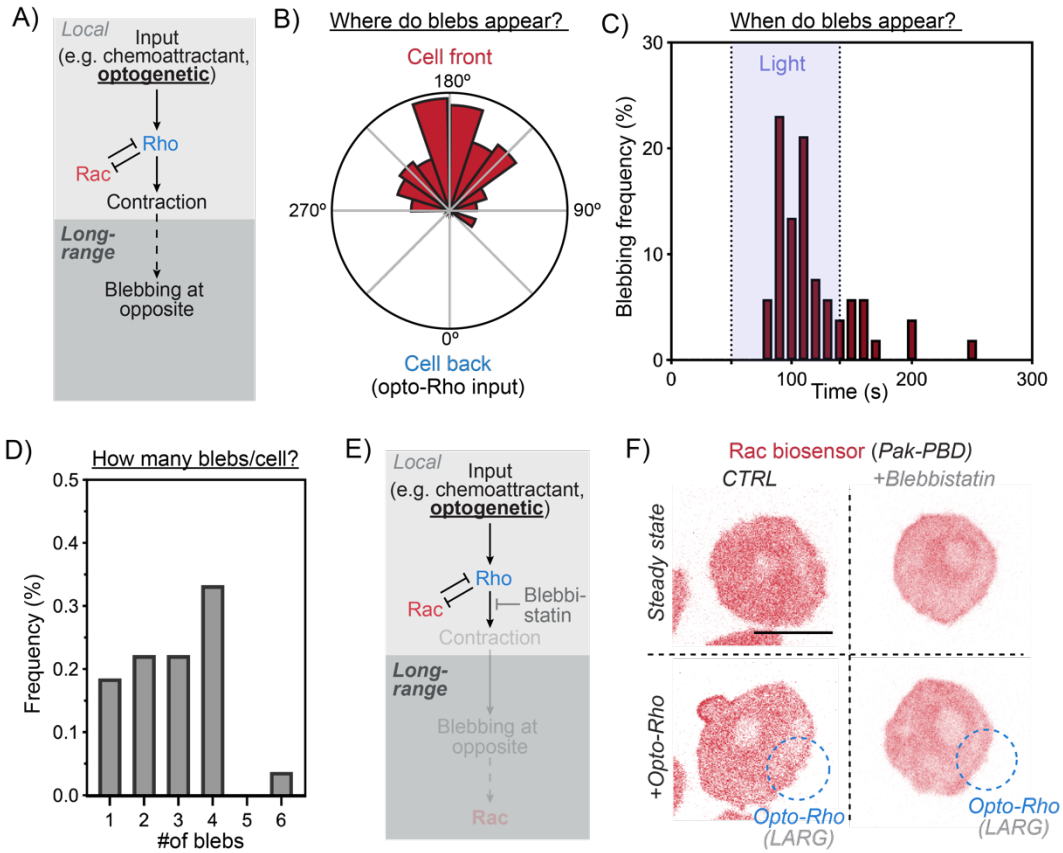


**Figure S4: Local Rho contraction leads to blebbing at the opposite side of the cell**

(A) Optogenetics-based local activation of Rho elicits blebbing at the opposite side of the cell. (B) Polar histogram of the spatial distribution of blebs appearance in relation to opto-Rho (cell back) showing that the majority of blebs are positioned at the opposite side of the cell back (opto-Rho). (N = 5, n > 65). (C) Histogram of bleb distribution in time during opto-Rho stimulation. (N = 3, n>55). (D) Histogram of the number of blebs per cell in response to opto-Rho stimulation (E) We locally activated Rho using optogenetics in the absence or presence of an inhibitor of myosin activation and blebbing (Blebbistatin). (F) Time-lapse confocal images of unpolarized cells expressing Rac biosensor Pak-PBD-mCherry and treated with 10uM of blebbistatin before and during opto-Rho stimulation. Scale bar: 10um.

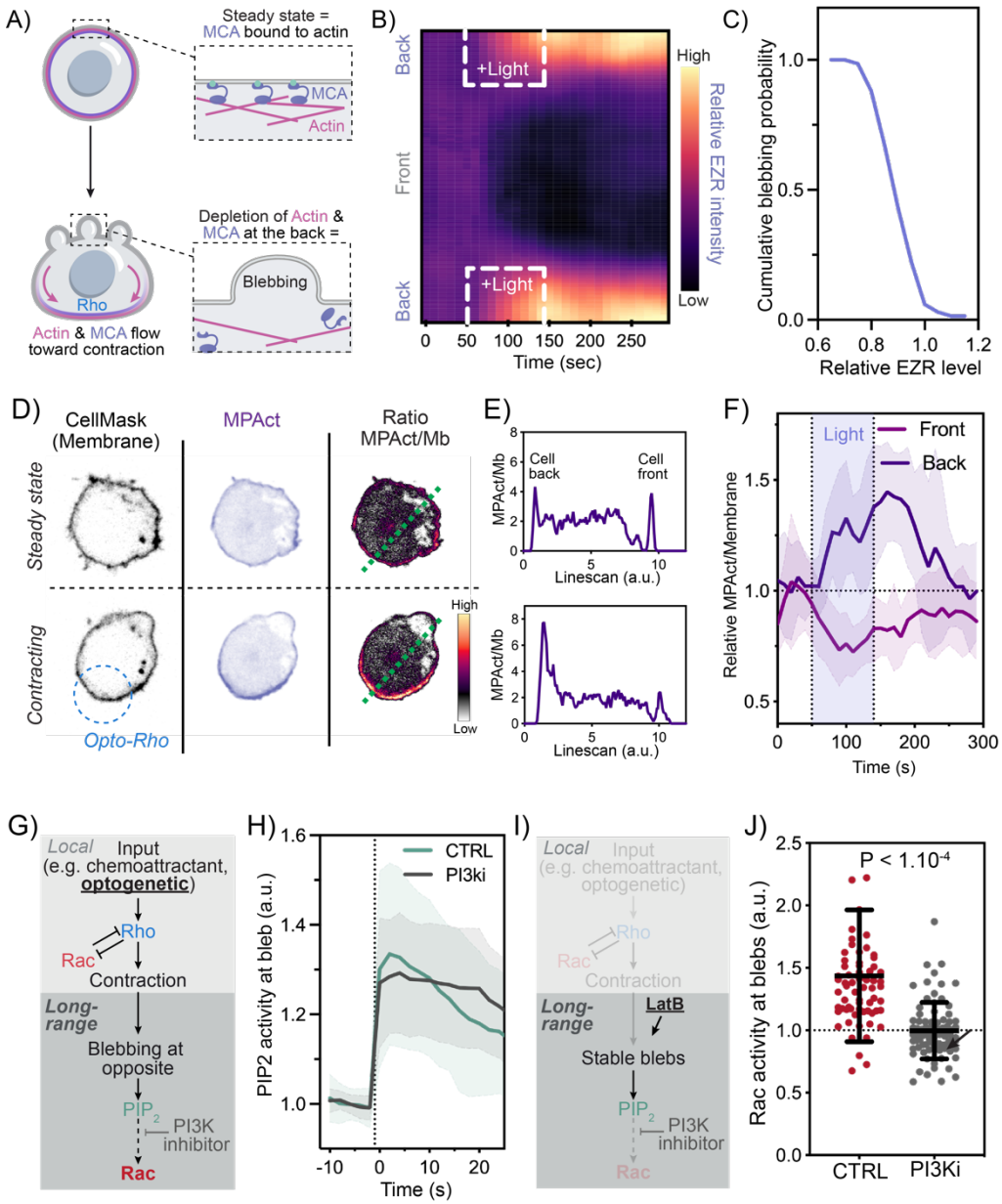


**Figure S5: Contraction-induced membrane-to-cortex attachment asymmetry leads to $PIP_2$ release and PI3K-dependent Rac activation at the opposite side of the cell**

(A) In unpolarized cells at steady state, actin and MCA proteins are uniformly distributed. Upon local contraction (for example induced by opto-Rho), Actin flows toward the site of contraction. We ask whether MCA flows with the cytoskeleton toward the site of contraction to generate an MCA asymmetry across the cell (B) Kymograph of Ezrin intensity along the normalized cell circumference (y axis) showing that over time (x axis), Ezrin is enriched at the back in response to opto-Rho activation. (C) Cumulative blebbing probability in function of relative Ezrin level. (N = 3, n >40). (D) Time-lapse confocal images of unpolarized cells expressing the MPact, a membrane-actin proximal sensor[39] which we use as a proxy for MCA level, and stained with the membrane marker CellMask before and during opto-Rho stimulation. The ratio between MPact and membrane channel is used to measure the approximative MCA level intensity. (E) Line-scan of MPAct/Membrane ratio of cell displayed in (D), see green dotted line. (F) Average time trace of relative MPAct/Membrane ratio

(normalized to before light) at the front and back of the cell. (N = 2, n >10, means ± SD). (G) Local Rho-induced contractions lead to MCA flow toward the site of contraction and depletion of MCA at the opposite end of the cell, resulting in blebbing at the cell pole that is opposed to opto-Rho. We hypothesized that MCA detachment from plasma membrane during blebbing leads to $PIP_2$ release. (H) Average time trace of $PIP_2$ activity at the bleb in control cells and cells treated with 1 uM PI3Kδ/γ inhibitor. (N = 3, n >30, means ± SD) (I) To determine whether blebs suffice for $PIP_2$-mediated Rac activation in a context independent of Rho-mediated stimulation of actomyosin contractility, we used the actin inhibitor Latrunculin B to generate stable blebs. (J) Rac activity in stable blebs in control cells and cells treated with 1 uM PI3Kδ/γ inhibitor show that PI3K inhibition prevents Rac activation in stable blebs. (N = 3, n >70, p values from Mann Whitney test).

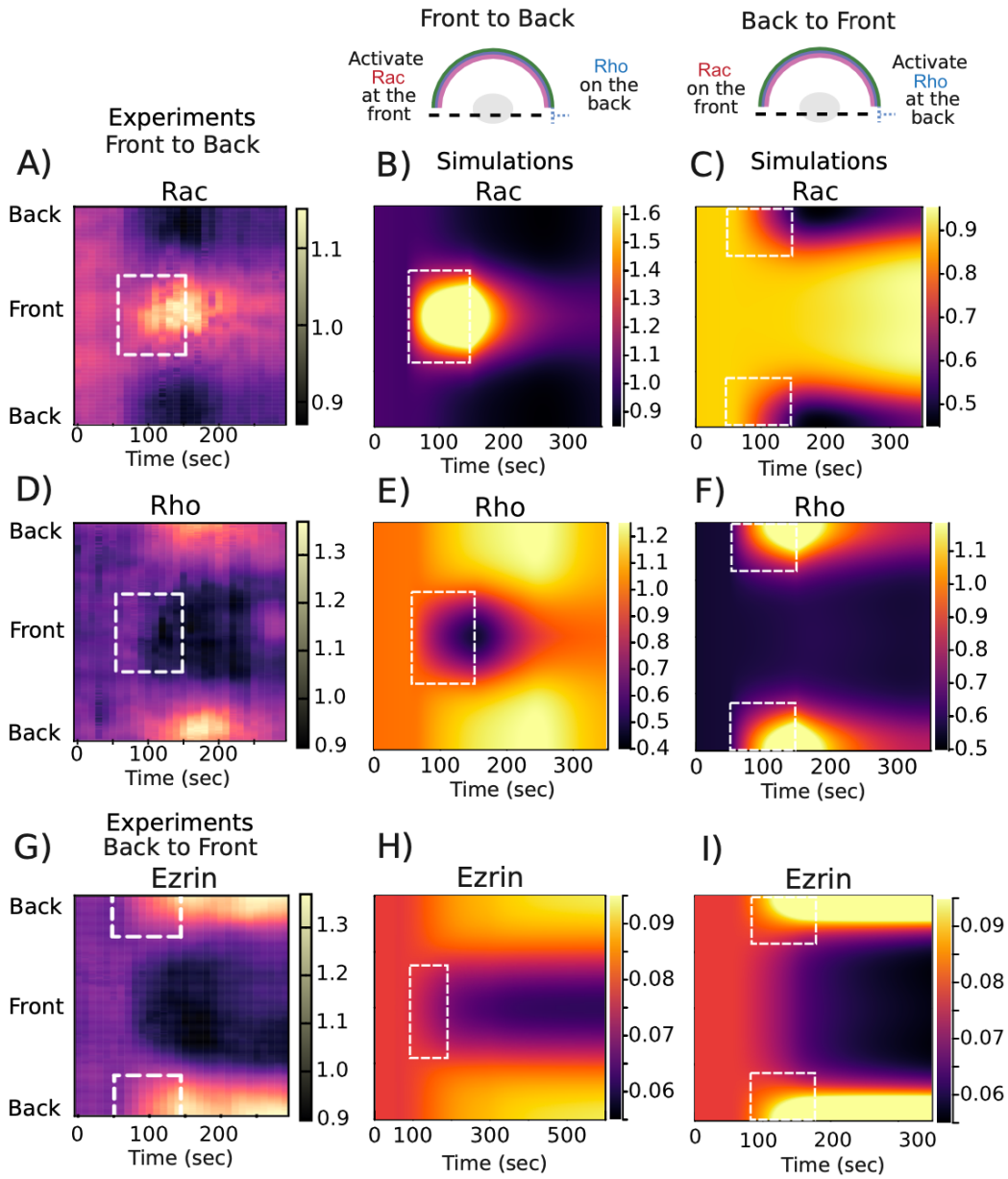


**Figure S6: Kymographs comparing experimental and simulated data.**
Kymographs from experiments and simulations for (A-C) Rac, (D-F) Rho, and (G-I) Ezrin. The first column (A,D,G) corresponds to experiments on both Front to Back and Back to Front. The second column (B,E,H) and third column (C,F,I) correspond to simulations results with Front to Back and Back to Front activation respectively. The dotted boxes correspond to the spatiotemporal window of activation of Rac or Rho, for Front to Back and Back to Front respectively.

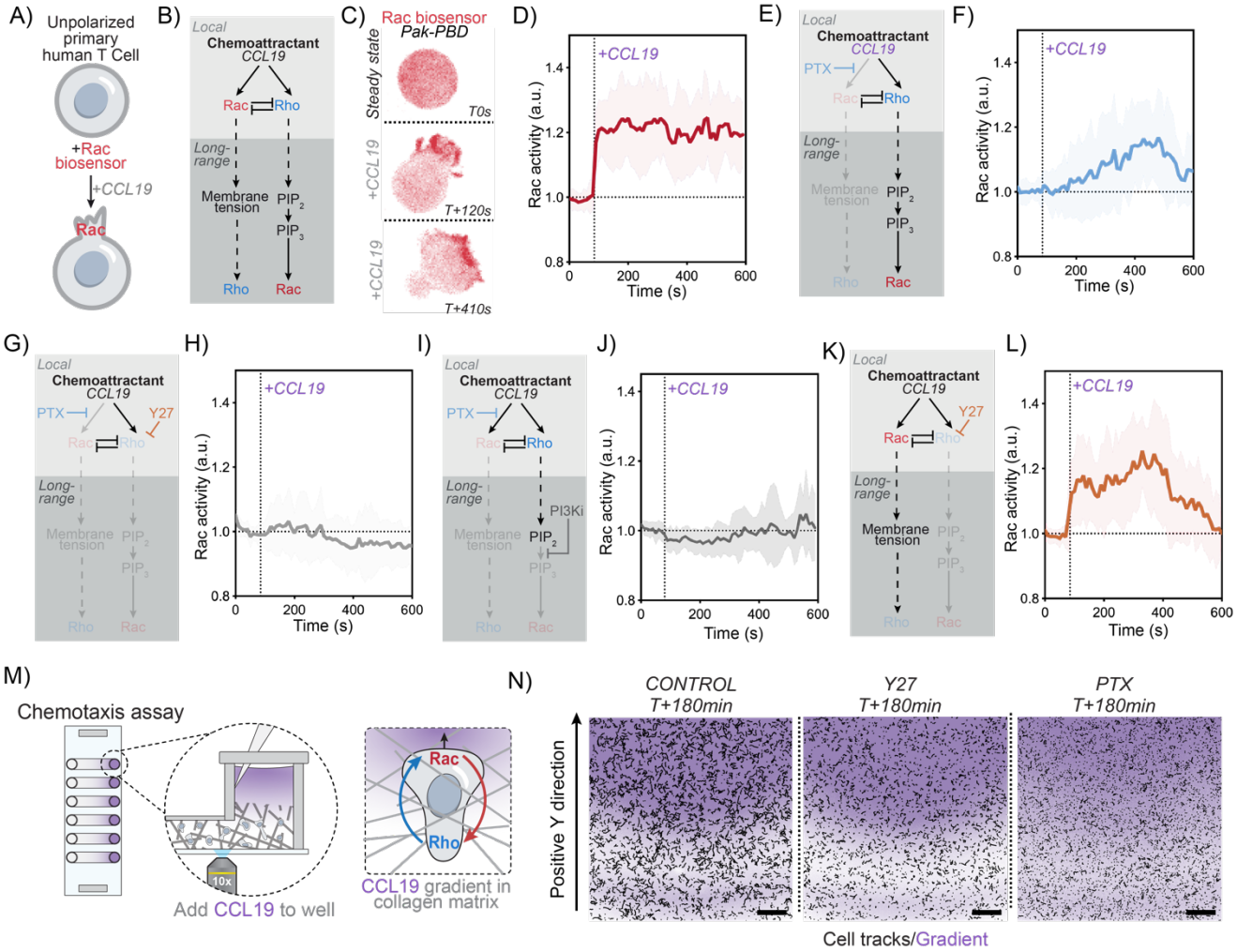


**Figure S7: Long range mutual activation establishes robust Rho and Rac polarity in primary T cells**

A) Primary human T cells expressing the Rac biosensor (Pak-PBD) to assay cell polarization following acute stimulation with the chemoattractant CCL19. B) CCL19 is known to activate both Rho and Rac. C) Time-lapse confocal images of an unpolarized human primary T cell before and during CCL19 stimulation. Rac activity was monitored via the Rac biosensor Pak-PBD. D) Average time trace of Rac activity at the cell front following addition of CCL19. (mean □SD; n>30, N= 3) E) Cells are treated with Gαi inhibitor PTX to prevent direct Rac activation by CCL19. F) Average time trace of Rac activity at the cell front of cells treated with 1 ug/ml of Gαi inhibitor following addition of CCL19. (mean □SD; n>20, N= 3). G) Cells are treated with a combination of Y27 and PTX to prevent direct Rho and Rac activation by CCL19. H) Average time trace of Rac activity at the cell front of cells treated with 1 ug/ml of Gαi inhibitor PTX together with 20uM of Y27 following addition of CCL19 (mean □SD; n>20, N= 3). I) Cells are treated with a combination of PTX and the PI3K inhibitor Duvelisib to disrupt the long-range Rho-mediated Rac activation described in this study. Average time trace of Rac activity at the cell front of cells treated with 1 ug/ml of Gαi inhibitor PTX together with 1uM PI3K inhibitor Duvelisib. (mean □SD; n>15, N = 2). K) Cells are treated with ROCK inhibitor Y27 to prevent Rho activation. L) Average time trace of Rac activity at the cell front of cells treated with 20uM of Y27 following addition of CCL19 (mean □SD; n>20, N= 3).Data for D), F), H) and L) is similar as in **Figure 7D** but separated

into different panels for extra clarity. (M) Ex-vivo assay for human primary T cell chemotaxis. Cells are premixed with Bovine Dermal Collagen and placed into linear channels. After collagen sets, media is added to one side of the channel (TCM) and media with human CCL19 (100ng total) and 10ug/mL of Dextran10k-AF647 (Dex647) is added to the other. Imaging takes place right on the edge of the well containing CCL19 so that T cell responses can be recorded as the CCL19 (as read out by Dex647) diffuses into the channel. (N) Representative control, Y27 and PTC experiment at 180s with Dex647 fluorescence and corresponding tracks of T cells; tracks display 3 minutes preceding timepoint listed.

## Material and Methods

### Experimental model and subject details

HL-60 cells are from the laboratory of Henry Bourne and were recently verified via STR profiling in[27] . HL-60s were cultured in R10 growth medium, which is RPMI 1640 supplemented with L-glutamine and 25 mM HEPES (Corning; Corning, NY) and containing 10% (v/v) heat-inactivated fetal bovine serum (Gibco; Waltham, MA). Cultures were kept at a density of 0.2–1.0 million cells/mL at 37°C/5% $CO_2$. HL60s knockouts for mSin1 and for mTORC2 were obtained from[27]. Opto-PI3K cells (iLid-BFP-CAAX, iSH2-GFP, Pak-PBD-mCherry) and Opto-LARG cells (iLid-BFP-CAAX, DHPH-ARHGEF1-GFP, AnillinRBD-mCherry) were obtained from[29,30]. Opto-PI3K and Opto-LARG expressing AnillinRBD-mCherry, Pak-PBD-mCherry, Ezrin-mCherry were assembled using a Golden-Gate-based modular cloning toolkit[69].

HEK293T cells (used to make lentivirus for transduction of HL-60s) are from UCSF cell culture facility (CCLZR076) and were grown in DMEM (Corning; Corning, NY) containing 10% (v/v) heat-inactivated fetal bovine serum (Gibco; Waltham, MA) and maintained at 37°C/5% $CO_2$. All media were 0.22-um filtered.

Healthy blood specimens from patients were obtained with informed consent according to the institutional review board-approved study protocol at the University of California - San Francisco (Study #21-35147). Volunteers were informed not to take ibuprofen, acetaminophen, or more than one drink of alcohol within 24 hrs, class 1 or 2 antihistamines within 5 days, or aspirin within 7 days of blood draw. Volunteer demographics such as age and sex are provided in the table below.

| Donor #: | Sex: | Age: |
|---|---|---|
| **4** | M | 28 |
| **21** | M | 28 |
| **23** | M | 24 |
| **28** | F | 27 |

### Method details

Making virus for transduction of HL-60 and primary T cells

HEK293T cells were used to generate lentivirus and were seeded into 6-well plates until approximately 80% confluent. For each transduction, 1.5 µg pHR vector (containing the appropriate transgene), 0.167 µg vesicular stomatitis virus-G vector, and 1.2 µg cytomegalovirus 8.91 vector were prepared for transfection using TransIT-293 Transfection Reagent (Mirus Bio; Madison, WI). Three days post transduction virus-containing supernatants were harvested and concentrated approximately 40-fold using Lenti-X Concentrator (Clontech; Mountainview, CA). Concentrated viruses were frozen and stored at −80°C until needed. For HL60s transductions (see below for T cell transduction), thawed virus was mixed with approximately 0.3 million cells in growth media supplemented with polybrene (8 µg/mL) and incubated overnight. Cells expressing desired transgenes were

isolated using fluorescence-activated cell sorting (FACS) as appropriate (BD FACSAria Fusion; BD Biosciences; Franklin Lakes, NJ).

T Cell isolation protocol:

Tcell Media (TCM) was first prepared with Lonza X-VIVO15 (Cat: 04-418Q), 5% human AB serum (Fisher, Cat#: NC9310328), 10 mM neutralized N-acetyl L-Cysteine (Sigma-Aldrich #A9165), and 1 mM 2-mercaptoethanol (Gibco #21985-023). Media mix was filtered and stored at 4C. Before use with Tcells, 40 U/mL human IL-2 (NCI BRB Preclinical Repository) was added in batches of 50mL and stored at 4C.

Blood specimens from patients were obtained with informed consent according to the institutional review board-approved study protocol at the University of California - San Francisco (Study #21-35147). Fresh samples of peripheral blood (3 tubes, 7 mL each) from healthy adult volunteers were collected via a BD 23-gauge butterfly needle collection set (Fisher SKU: 23-021-022) into 8.5 ml BD Vacutainer ACD Solution A tubes (BD364606). Blood was kept on a shaker at minimum setting and utilized within 2 hours of the draw. CD4+ Tcells were isolated using the Stemcell EasySep Direct Human CD4+ Tcell Isolation Kit (#19662) with the Easy50 magnet (#18002) according to the manufacturer's protocol. Cells were spun down at 300g for 5min, resuspended in TCM + 40 U/mL IL-2 between 1-2 x 10^6 cells/mL, and then placed in a Corning 6 well plate (CAT). For drop assay use, T cells went through the transduction protocol below; for chemotaxis use they followed the chemotaxis protocol from this point. For all language used in this method section, day 1 is the day of isolation.

Transduction of human primary T cells:

To integrate the biosensors into the primary Tcells, we did the following protocol. Tcells were allowed to rest in IL-2 TCM overnight until activation midday on Day 2. To activate the Tcells, cells were placed in a 24 well plate with approximately 1-1.5x10^6 cells per well in 1mL of media. Next, following the manufacturer's guidelines, we added 25uL of washed and TCM + 40U/mL IL-2 resuspended CD3/28 Dynabeads (Gibco, Cat#: 11131D) to each well. Cells were incubated with beads for 24 hours before being transferred to a 24 well plate pre-coated with retronectin (Takara, Cat#: T100B). Retronectin coating was done by following the manufacturer's protocol with approximately 10ug/well (5ug/cm^2) used in 0.5mL of PBS in Falcon nonTC treated 24 wells (Cat# 0877251). Next, 100uL of concentrated lentivirus was added to each well of Tcells for the Rac-mCherry biosensor. Normally, three or four wells of the same condition were used in parallel in order to have enough cells to sort. Cells were spin-fected by spinning at 460g for 1 hour at room temperature (25-30C), and then placed in a 37C 5% CO2 incubator for 3 days. On day 6, cells were taken from the plate, Dynabeads were removed with a magnet, then placed in a fresh tube. Cells were then spun down at 300g for 5 min, resuspended in fresh TCM with 40U/mL IL-2 at approximately 2 x 10^6 cells/mL. Cells were sorted for positive mCherry fluorescence on a FACSAria Fusion instrument. After sorting, cells were spun down and resuspended in fresh TCM + 40 U/mL of IL-2. Cells were allowed to rest for two or more days before use in drop experiments.

Microscopy hardware

Imaging depicted in Figure 1-5 and S1-6 were performed at 37°C on a Nikon Eclipse Ti inverted microscope equipped with a Borealis beam conditioning unit (Andor), a CSU-W1 Yokogawa spinning disk (Andor; Belfast, Northern Ireland), a 100X PlanApo TIRF 1.49 numerical aperture (NA) objective (Nikon; Toyko, Japan), an iXon Ultra EMCCD camera (Andor), and a laser merge module (LMM5, Spectral Applied Research; Exton, PA) equipped with 405, 440, 488, and 561-nm laser lines. All hardware was controlled using Micro-Manager (UCSF).

Optogenetic activation was performed using a LED (470-nm) via a custom DMD (Andor Technology). Illumination intensities were varied by connecting the LEDs to the analog outputs of a digital-to-analogue converter and setting the LED voltages using serial commands via custom Python code. The microscope is equipped with two stacked dichroic turrets such that samples can be simultaneously illuminated with LEDs and imaged using a 488-nm long-pass dichroic filter (Chroma Technology Corp.)

Imaging depicted in figure 7 were performed using a Nikon Ti2-E body scope configured with a CrestOptics X-Light V3 confocal spinning disk system, a Lumencor Celesta light engine, Nikon 10x CFI Plan Apo Lambda objective, an Okobox temperature and $CO_2$ controlled environment, and a Photometrics Kinetix sCMOS camera. The camera was run in a 2x2 binning mode with a set exposure time of 200 ms for all channels. All videos are taken with a frame interval of 30 seconds between exposures unless otherwise indicated. All videos were taken at 37°C with 5% CO2 for the duration of imaging.

Preparation of Opto-PI3K and Opto-LARG cells for confocal imaging

For experiments in which we monitored cells by confocal imaging, cells were seeded in a 96-well #1.5 glass-bottom plates (Azenta Life Sciences) in R+B imaging media, which is RPMI 1640 supplemented with L-glutamine and 25 mM HEPES (Corning; Corning, NY) and containing 0.2% Bovine Serum Albumin (BSA, endotoxin-free, fatty acid free; A8806, Sigma; St. Louis, MO). For optogenetic activation, cells were illuminated using DMD (see above) at a chosen location (using custom Python code) in a circular pattern of varying size (~2 microns radius for Opto-PIK, ~1 micron radius for Opto-LARG) for a duration of 90 seconds.

For plasma membrane imaging using the membrane dye CellMask (Figures 1F, 1G , 2D, 2G, 2H, 2K, 2L, 3B, 3C, 3E, 3F, 3H, 3I), cells were first incubated with ~2-5μg/ml of CellMask™ Deep Red (C10046, Thermofisher) for 3 minutes at 37°C/5% $CO_2$. Cells were then pelleted at 300*g* for 3 min and resuspended in R+B imaging media (RPMI+0.2% BSA). For actin imaging using HaloTag (Figure S1E, F), cells were stained with 100nM of JF646X for 10 min before being pelleted at 300*g* for 3 min and resuspended in R+B imaging media (RPMI+0.2% BSA).

Osmotic shock

For osmotic shock experiments cells were stained using CellMask™ Deep Red (see above) and seeded in a 96-well #1.5 glass-bottom plates (Azenta Life Sciences) in R+B imaging media, which is RPMI 1640 supplemented with L-glutamine and 25 mM HEPES (Corning;

Corning, NY) and containing 0.2% Bovine Serum Albumin (BSA, endotoxin-free, fatty acid free; A8806, Sigma; St. Louis, MO). Deionized water was then manually added at different amount (50-80% of the final volume, depending) while imaging.

Micropipette aspiration

Micropipette aspiration experiments depicted in Figure 2 and figure 3 were performed using a micromanipulator (Narishige MM-188NE) mounted on Nikon Eclipse Ti (detailed description above) using a custom 3d printed mount. The micropipettes (Sunlight Medical Inc, SRP-05P-35) were mounted and secured onto the holder using polystyrene foam. Aspiration was performed manually using the CellTram 4r air (eppendorf) . Micropipettes were coated for 10min with RPMI containing 5% BSA to prevent cells sticking to it. The media was then emptied, and the pipette filled with R+B imaging media (RPMI+0.2% BSA) for about 30-60min. Cells were plated on round MateK dishes in R+B imaging media (RPMI+0.2% BSA). Aspiration was monitored live using both brightfield and the membrane dye CellMask™ Deep Red (see above for staining protocol).

Stable blebs

For stable blebs generation (Fig 4J, K & S5M), cells were seeded on imaging plates pre-coated with poly-l-lysine (Sigma-Aldrich, P4832) (coated for 5min and washed three times with PBS). Imaging media used was R10 growth medium, which is RPMI 1640 supplemented with L-glutamine and 25 mM HEPES (Corning; Corning, NY) and containing 10% (v/v) heat-inactivated fetal bovine serum (Gibco; Waltham, MA) together with 10μM of Latrunculin B (Sigma-Aldrich, 76343-94-7).

Pharmacological treatments

For inhibition of cellular protrusion (Figure 2C, D & S2A-C), cells were seeded in imaging media (RPMI 1640 supplemented with L-glutamine and 25 mM HEPES (Corning; Corning, NY) and containing 0.2% Bovine Serum Albumin (BSA, endotoxin-free, fatty acid free; A8806, Sigma; St. Louis, MO), supplemented with either 10μM of Latrunculin B (Sigma-Aldrich, 76343-94-7) or 100μM of CK666 (Sigma-Aldrich, 442633-00-3). For inhibition of the actin cortex during osmotic shock (Figure S2H), cells were seeded in imaging media (as described above) supplemented with 10μM of Latrunculin B (Sigma-Aldrich, 76343-94-7). H20 also containing 10μM of Latrunculin B was then added during imaging to generate an hypoosmotic shock without diluting the drug. Inhibition of mTOR kinase activity (Figure S3C-E) was performed by treating cells with 1-5 μM of KU-00636794 (Selleck Chemical LLC, 50-837-4) for 30-40min prior imaging. For inhibition of contractility (Figure 4G & S4G), cells were seeded in imaging media supplemented with 10μM of the blue light resistant para-amino-Blebbistatin (Cayman Chemical, 22699). For PI3Kδ/γ inhibition (Figure 5E, S5K & S7), cells were seeded in imaging media supplemented with 1μM Duvelisib (Medchemexpress LLC, NC2099793). For inhibition of Rho activity in human primary cells (Figure S7), cells were seeded in T cell starvation media consisting of Lonza X-VIVO15 (Cat: 04-418Q), 0.4% Bovine Serum Albumin (Sigma-Aldrich, 9048-46-8), 10 mM neutralized N-acetyl L-Cysteine (Sigma-Aldrich #A9165), and 1 mM 2-mercaptoethanol (Gibco #21985-023). Media mix was filtered and stored at 4C. Before use with Tcells, 40 U/mL human IL-2 (NCI BRB Preclinical

Repository) was added in batches of 50mL and stored at 4C. T cell starvation media was supplemented with 20μM of Y-27632 (MilliporeSigma, 68-800-01MG). For inhibition of Gαi signaling (Figure 7C), cells were incubated overnight in media (starvation for CCL19 drop experiments and culture media for migration experiments) supplemented with 1μg/ml of Pertussis toxin (Thermo Fischer Scientific, PHZ1174)

CCL19 drop assay

For CCL19 drop assay (Figure 7A-D & S7), human primary cells were serum starved overnight in serum starvation media consisting of Lonza X-VIVO15 (Cat: 04-418Q), 0.4% Bovine Serum Albumin (Sigma-Aldrich, 9048-46-8), 10 mM neutralized N-acetyl L-Cysteine (Sigma-Aldrich #A9165), and 1 mM 2-mercaptoethanol (Gibco #21985-023). Media mix was filtered and stored at 4C. Before use with Tcells, 40 U/mL human IL-2 (NCI BRB Preclinical Repository) was added in batches of 50mL and stored at 4C. Cells were then seeded on 96-well #1.5 glass-bottom plates (Azenta Life Sciences) pre-coated for 30 min with human fibronectin at 1mg/ml (Sigma-Aldrich, F0895). During imaging, starvation media containing 50mM of CCL19 (R&D Systems, 361MI025CF) was added into the well after 90 sec of imaging. To avoid unwanted dilution, drugs such as Y27 and Pertussis toxin (PTX) were also added to the CCL19 mix at the same concentration as used during cell plating.

T Cell migration Experimental Preparation:

On the day of experiment, an ibidi 6 channel device was assembled by sticking down a sticky-Slide VI 0.4 (ibidi, Cat: 80608) to a bare 1.5H full coverslip (ibidi, Cat:10812). Care was taken not to press too hard on the device, and a P1000 tip was taken to gently press out air bubbles between the adhesive and glass. The device was placed at 37C until use to set. Devices that were not fully used were emptied, the used channel marked and put in the fridge at 4C for use of unused channels within a week.

Unactivated human Tcells were allowed to culture in TCM + 40U/mL IL-2 until day 5-6 before use in the chemotaxis assay. On the day of the assay, 5 μg/ml of Hoechst 3334 (Invitrogen, Cat:H3570) was added directly to the culture media for 15 min at room temperature. Cells were then spun down, resuspended in fresh in TCM + 40U/mL IL-2 at around 5x10^6 cells/mL and put on ice.

Next, we prepared a collagen solution at a 2x concentration to mix with the cells. All steps were carried out on ice until indicated, and the ibidi chip was placed on to an icepack block to get cold before use. First, 18uL Type I Bovine Collagen Solution (Nutragen Cat No. 5010-50ML) was pipetted into an ice cold 1.5mL Eppendorf tube with a positive displacement pipette. Next, 12uL of FITC-collagen (Sigma, Cat: C4361-10ML) was added and mixed with a positive displacement pipette on ice. Following a decent mixture of the two, 14uL of ice cold MilliQ filtered water and 10uL of ice cold 55mM NaOH were added and mixed with a normal pipette on ice. The entire 60uL collagen solution was mixed 1:1 with the chilled concentrated cell solution above and then 100uL of this collagen/cell mix was immediately injected into a channel of the cold ibidi device. Usually two channels were loaded (control and drug) and the device was left on ice until both channels were loaded. Care was taken to ensure that an even amount of collagen/cell mix was distributed to each side of the channel before the

entire device was placed on top of a heat block inside of a 37C, 5% CO2 incubator. The device was allowed to incubate for 30min before use in microscopy experiments.
For imaging, the ibidi channel device was moved to the microscope described in microscopy hardware for Figure 7. While incubating at 37C and 5% CO2, 50 uL of TCM + 40U/mL of IL-2 was added to one side of the channel and 50uL of TCM + 40 U/mL of IL-2 + 5-10ug/mL of 10kDa AF647-Dextran (Invitrogen, Cat#: D22914) + 200nM recombinant human CCL19 (Biotechne, Cat#: 361-MI) was added to the other side. Imaging occurred on the edge of the channel port that had the CCL19 added to it.
When drugs were used in this assay, the correct and final treatment concentration was added to all parts of the assay so that the concentration listed in the text was present in the collagen, media, and chemoattractant mixes.

**Quantification and statistical analysis**

Image and membrane tension analysis
Fiji (NIH)[70], Excel (Microsoft; Redmond, WA), custom Python code, and Prism (Graphpad software, Inc) were used for image analysis.

For average Rac activity (Pak-PBD), Rho activity (AnillinRBD) or Ezrin intensity in opto-PI3K cells (Figure 1C, 1D, 1F, 1G, S1C, S1F, S1I, 2D, 3B, 3C, S5C, 5D) cells were automatically segmented using CellPose[71]. We then generated kymographs by segmenting the cell body through either the CellMask channel and finding the three-pixel wide boundary pixels that best capture the membrane of the CellMask channel. We then confirmed that our segmentation pipeline could function equally well using directly the Rac, Ezrin or Rho biosensors signal, thus avoiding potential bleed through from the membrane stain. The segmented cell is unraveled, and AnillinRBD, Pak-PBD or Ezrin intensity are measured and stored in an array. For kymographs (Figure S1C, S1F, S1I, S5D) arrays were stacked to show the evolution of the signal over time. For line graphs (Figure 1C, 1D, 1F, 1G, 2D, 3B, 3C, S3E, S5C), the array was then divided into four separate quadrants (front, sides and back), aligned to the opto-PI3K input which we defined as the cell front. Average fluorescence per quadrant was then computed for each quadrant of each cell. All measurements were then normalized per cell to steady state. Image segmentation code utilized the Python package Scikit-Image[61]
.
For plots of Rho activity during osmotic shock (Figure 2H, S2E, S2H, 3F) and for plots of Rho activity during micropipette aspiration assays (Figure 2L, 2J, 3I, S3J) we used a custom Fiji macro which uses the membrane channel (CellMask) to create a mask of the cell membrane which is then used to measure the average AnillinRBD levels at the cell membrane. All measurements were then normalized per cell to steady state. For figure 2L and 3I, we used 30 seconds before aspiration for steady state, 30 seconds of active aspiration.

Average Rac activity (Pak-PBD) and PIP2 levels in blebs during opto-contraction (Figure 4D, 4G, S5K, 5C, 5D), were acquired by manually segmenting blebs using the membrane signal. We then backtracked in time to measure the fluorescence at the same patch membrane of membrane before it blebbed to obtained steady state measurements. For cells without

blebs (Figure 4G, grey), we measured a Rac activity at the patch of membrane directly opposite of the opto-light.

For fig S4B-D. We measured bleb angle in relation to the activating light using the angle tool in Fijii as well as record when blebs first appear in response to light for Fig S4C. Angles were then computed using python and Scikit-Image[72].

For stable blebs, in figure 3K and S3M, me measured average Pak-PBD activity at blebs and in an adjacent patch of membrane as reference. File names for control and PI3Ki cells were randomized, and analysis was performed blind.

For figure S5H and S5I we used a custom Fijii macro to measure the ratio of the MPAct and the membrane channel (CellMask) using a blurred membrane channel as a mask to only perform the ratio near the plasma membrane. We then measured the MPAct/Membrane ratio at the cell front and back (defined by the location of the opto-light) over timer. We then normalized every cell to their steady state.

For figure 7D, we measured average Rac activity at the cell front by manually identifying cell protrusions using a fluorescence Z-stack together with brightfield imaging. We then backtracked pre-CCL19 drop to measure Rac activity at the same patch of membrane to obtained steady state measurements. When a front could not easily be identified, we measured Rac activity at the membrane of the mid-plane of the cell. Because only some of cells express CCR7 (approx. 7-80%), the receptor for CCL19, we only included in the analysis cells that displayed a cell shape change in response to CCL19 (protrusion, contraction, blebbing, migration etc.).

For figure 7G-J The T cell chemotaxis image analysis presented in this work was achieved via the use of both Fiji (ImageJ) and Python. Images were pre-processed in Fiji by max projecting the z-stack of nuclei taken to simplify the downstream Python analysis. Nuclei were segmented using StarDist, and labeled nuclei were linked into tracks using the scikit-image and TrackPy packages. Tracks were then analyzed for their step-wise linear velocity and velocity X and Y bias over time. All python analysis for each graph will be provided as open-source code in the form of both scripts and Jupyter notebooks on Github by the time of publication.

<u>Statistical analysis</u>

For all statistical analysis, PRISM 9 (Graphpad software, Inc) was used. Statistical details can be found in the legend of each figure. N represents number of independent biological replicates. Pooled independent experiments are used in dot plots. Error bars always represent SD.

# Key resources table

**Key resources table**

| **REAGENT or RESOURCE** | SOURCE | IDENTIFIER |
|---|---|---|
| Chemicals, peptides, and recombinant proteins | | |
| RPMI 1640 supplemented with L-glutamine and 25 mM HEPES | Corning | 10-041-CM |
| Bovine Serum Albumin (endotoxin-free, fatty acid free) | Sigma-Aldrich | A8806 |
| Heat-inactivated fetal bovine serum | Gibco | 16140071 |
| DMEM | Corning | 10-017-CV |
| Bovine Calf Serum | Sigma-Aldrich | 12138C |
| Latrunculin B | Sigma-Aldrich | 76343-94-7 |
| KU 0063794 | Selleck Chemical LLC | 50-837-4 |
| CK-666 | Sigma-Aldrich | 442633-00-3 |
| Para-Amino-Blebbistatin | Cayman Chemical | 22699 |
| Duvelisib | Medchemexpress LLC | NC2099793 |
| Recombinant Human CCL19/MIP-3 beta Protein | R&D Systems™ | 361MI025CF |
| Y-27632 | MilliporeSigma | 68-800-01MG |
| Pertussis Toxin | Thermo Fischer Scientific | PHZ1174 |
| CellMask™ Deep Red | Thermofisher | C10046 |
| Janelia Fluor 646 | Janelia | JF646X |
| Lenti-X Concentrator | Clontech | 631231 |
| TransIT-293 Transfection Reagent | Mirus Bio | MIR2705 |
| 96-well #1.5 glass-bottom plates | Azenta Life Sciences | 4ti-0223 |
| Non-Clinical Micropipettes, ID5.0um, flat polished 35 | Sunlight Medical Inc | SRP-05P-35 |
| **Experimental models: Cell lines** | | |
| HL60s | Bourne lab | |
| Opto-PI3K HL60s | Weiner lab | |
| Opto-LARG HL60s | Weiner lab | |
| mSIN1 KO HL60s | Weiner lab | |
| Rictor KO HL60s | Weiner lab | |
| HEK293T | UCSF cell culture facility | CCLZR076 |

| **Software and algorithms** | | |
|---|---|---|
| Fiji | [59] | N/A |
| Prism 9 | Graphpad software, Inc | N/A |
| Adobe Illustrator | Adobe | N/A |
| Excel | Microsoft | N/A |

# Supplementary text

Henry De Belly, Andreu Fernández Gallén, Evelyn Strickland, Dorothy C. Estrada, Patrick J. Zager, Janis K Burkhardt, Hervé Turlier, Orion D. Weiner

October 2024

## 1 Model hypotheses

Rho GTPases have emerged as key components of the cell polarization machinery. Among them, Rho and Rac are well-known for their antagonistic and inhibitory relationship, often modeled through reaction-diffusion equations [1]. A well-established paradigm for cell polarization is the concept of wave-pinning [2], where bistability of a single RhoGTPase arises from the interplay between a degradation term and a non-linear activation term, combined with overall mass conservation. Recent models have also incorporated the experimentally observed dependence of Rho on membrane tension [3, 4].

In our model, we propose an alternative polarization mechanism to wave-pinning, in which we neglect the shuttling between active and inactive forms of Rho GTPases. Instead, we model the local mutual inhibition between Rho and Rac [5] as a bistable switch, which naturally exhibits both monostable and bistable regimes, depending on the parameter set [6]. The couplings between cortical and membrane mechanics are the essential components that enable cell polarization, and we have designed these based on experimental observations. Similar to previous works [3, 4], and in agreement with our experimental findings, we assume that increased membrane tension promotes RhoA activation.

Our minimal mechanical model integrates the membrane and cortex based on previous work by some of the authors [7]. In this model, membrane tension effectively acts as a tangential elasticity (membrane folding/unfolding), while the cortex is represented as a viscous, contractile layer [8, 9, 10]. Their mechanical interaction is implemented through viscous friction, which slows their relative tangential movement. This leads to effective diffusive propagation of membrane tension along the cell surface [11], which homogenizes in neutrophils after perturbations over timescales longer than several minutes [7].

In our current work, we refine this model by explicitly accounting for the spatiotemporal variations in membrane-cortex attachment (MCA) surface density, particularly of ezrin, which exchanges with its inactive form in the cytoplasm and can be advected by cortical flows. Experimentally, we further observe that protrusions through blebbing are enhanced in regions of the membrane with low MCA and include this key coupling minimally via a switch-like dependence of the protusion velocity with MCA density.

After describing the biochemical model for Rho and Rac, we derive coupled equations for our minimal mechanochemical model in one dimension and simulate it using the finite-element method.

## 2 Biochemical model of Rho and Rac

In this section, we first describe the coupled dynamics of Rac ($a$) and Rho ($b$), modeled locally via ordinary equations describing their activation modulated by mutual inhibition and their inactivation, in a similar fashion as a toggle-switch [12]. In contrast to wave-pinning models, which account explicitly for the shuttling between an active form of the protein in the membrane and an inactive form in the cytosol, and rely importantly on a limited total amount of RhoGTPase in the cell, we assume here the membrane in contact with a chemiostat of inactive proteins in the cytosol. As such, we assume effectively a constant cytosolic concentration, that is integrated within the activation rates. This simplifying hypothesis is justified by former experimental work, which demonstrated that in neutrophils, a diffusion-based inhibition or local sequestration mechanism was not sufficient to explain polarization [13].

The two ordinary equations read

$$\frac{\partial a}{\partial t} = \alpha_0 \frac{k_a^2}{k_a^2 + b^2} - d_a a, \tag{1}$$

$$\frac{\partial b}{\partial t} = \beta_0 \frac{k_b^2}{k_b^2 + a^2} - d_b b, \tag{2}$$

where $\alpha_0$ and $\beta_0$ are the basal activation rates of Rac ($a$) and Rho $b$, respectively; $k_a$ and $k_b$ set the switch threshold values for $a$ and $b$.

## 2.1 Non-dimensionalized equations

We non-dimensionalize previous equations defining dimensionless protein concentrations

$$\bar{b} = b/k_a \tag{3}$$

$$\bar{a} = a/k_b \tag{4}$$

and dimensionless activation rates

$$\bar{\alpha}_0 = \frac{\alpha_0}{k_b\, d_a}, \tag{5}$$

$$\bar{\beta}_0 = \frac{\beta_0}{k_a\, d_b}. \tag{6}$$

The resulting dimensionless equations for the biochemical equations are

$$\frac{1}{d_a}\frac{\partial \bar{a}}{\partial t} = \bar{\alpha}_0 \frac{1}{1+\bar{b}^2} - \bar{a}, \tag{7}$$

$$\frac{1}{d_b}\frac{\partial \bar{b}}{\partial t} = \bar{\beta}_0 \frac{1}{1+\bar{a}^2} - \bar{b}. \tag{8}$$

## 2.2 Steady-state solutions

**Nullclines and fixed points**

Steady-state equations ($\partial/\partial t = 0$) define the nullclines

$$0 = \bar{\alpha}_0 \frac{1}{1+\bar{b}^2} - \bar{a} \equiv f(\bar{a}, \bar{b}), \tag{9}$$

$$0 = \bar{\beta}_0 \frac{1}{1+\bar{a}^2} - \bar{b} \equiv g(\bar{a}, \bar{b}). \tag{10}$$

The intersection of the nullclines $f(\bar{a}, \bar{b})$, $g(\bar{a}, \bar{b})$ define the possible steady-state solutions as function of the values of activation rates $(\bar{\alpha}_0, \bar{\beta}_0)$. As illustrated on Fig. 1, there are two possible scenarios. Either the nullclines have one intersection - or fixed - point, which is always a stable solution, and corresponds either to a (high Rac/low Rho), or (low Rac/high Rho) situation; or the curves intersect on three fixed points, two of which are stable solutions while the intermediate one is unstable. In the former case, the system is said monostable, while in the latter, the system displays a bistable behavior where both (high Rac/low Rho) and (low Rac/high Rho) coexist as possible stable solutions.

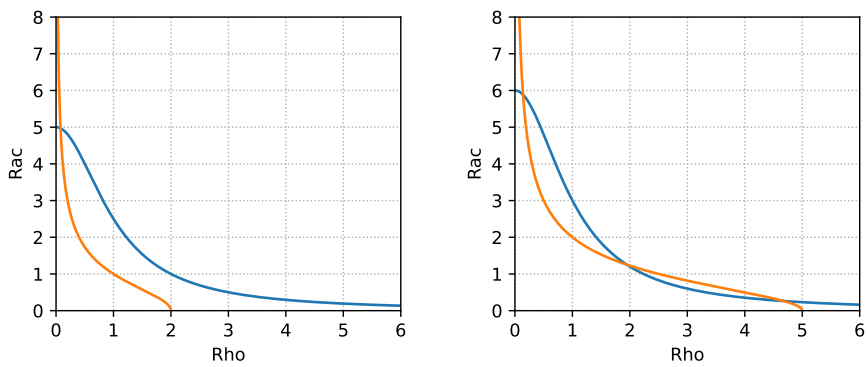


Figure 1: Plot of eqs (9) and (10) for the values $\bar{\alpha}_0 = 5$ $\bar{\beta}_0 = 2$ and $\bar{\alpha}_0 = 6$ $\bar{\beta}_0 = 5$ respectively. There is a steady state solution for $a$ and $b$ where this two lines cross.

**Phase diagram**

We can compute the regions of parameters $(\bar{\alpha}_0, \bar{\beta}_0)$ of monostability and bistability by looking for the roots $(\bar{a}^*, \bar{b}^*)$ of the steady-state equations $(f(\bar{a}, \bar{b}) = 0,\ g(\bar{a}, \bar{b}) = 0)$, while ensuring that these roots are stable fixed points $(\partial_{\bar{a}} f(\bar{a}, \bar{b})|_{\bar{a}^*, \bar{b}^*} < 0\ \partial_b g(\bar{a}, \bar{b})|_{\bar{a}^*, \bar{b}^*} < 0)$.

The transition lines between monostable and bistable stability regions are obtained when

$$f(\bar{a}, \bar{b}) = 0, \quad g(\bar{a}, \bar{b}) = 0, \quad \partial_{\bar{a}} f(\bar{a}, \bar{b}) = 0, \quad \partial_{\bar{b}} g(\bar{a}, \bar{b}) = 0, \tag{11}$$

which leads to the following polynomial equations for $(\bar{a}, \bar{b})$

$$0 = -\bar{\alpha}_0 + \bar{a}\left(1 + \bar{\beta}_0^2\right) - 2\,\bar{a}^2\bar{\alpha}_0 + 2\,\bar{a}^3 - \bar{a}^4\bar{\alpha}_0 + \bar{a}^5 \tag{12}$$

$$0 = -\bar{\beta}_0 + \bar{b}\left(1 + \bar{\alpha}_0^2\right) - 2\,\bar{b}^2\,\bar{\beta}_0 + 2\,\bar{b}^3 - \bar{b}^4\,\bar{\beta}_0 + \bar{b}^5 \tag{13}$$

The phase diagram is plotted on Fig. 2 as function of $\bar{\alpha}_0$ and $\bar{\beta}_0$.

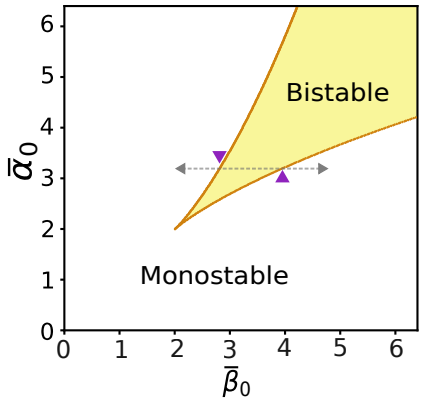


Figure 2: Phase diagram of mono and bi-stability regions of Rho and Rac, as function of their normalized activation rates $\bar{\beta}_0$ and $\bar{\alpha}_0$. The transition curves are in orange. Plotted in grey arrow the hysteresis represented in Figure 3 for the line $\bar{\alpha} = 3.2$ and represented and with purple triangles each transition point for the hysteresis.

The transition from low to high Rho/Rac and conversely exhibits a hysteresis, that we illustrate on Fig. 3. At a given value $\bar{\alpha}_0 = 3.2$, if one increases $\bar{\beta}_0$ from a low value $\sim 0$, the system will switch from (high Rac, low Rho) to (low Rac, high Rho) only when $\bar{\beta}_0$ reaches the second transition curve at $\bar{\beta}_0 \simeq 3.92$. Traversing the parameter space in the reverse direction, starting from $\bar{\beta}_0 \sim 6$ and decreasing its value the transition from (low Rac, high Rho) will happen this time when goes below $\bar{\beta}_0 \simeq 2.82$

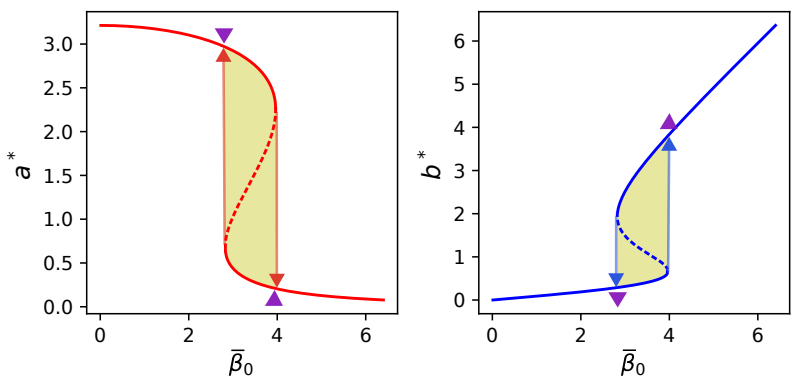


Figure 3: Steady-state solutions of Rac $a^*$ and Rho $b^*$ as function of $\bar{\beta}_0$ ($\bar{\alpha}_0 = 3.2$ being constant). The solid lines represent stable solutions while the dotted line represents unstable solutions. The hysteresis is materialized through arrows, which delimits the bistability region in yellow $\bar{\beta}_0 \in [2.82, 3.92]$. The purple triangles pointing up and down correspond to the transition line points depicted on Fig. 2.

## 2.3 Hysteresis and sensitivity to initial conditions

In the bistable region, the hysteresis manifests itself in the dependence on the stationary solutions on the initial conditions and type of activation.

Starting from a high Rho state (initial condition $\gamma$ on Fig. 4), a local overactivation of Rac can induce a spatial segregation of Rho and Rac, whereas the same overactivation of Rac starting from a high Rac state will not induce polarisation.

This illustrates the inability of the local inhibition model alone to spontaneously and robustly polarize depending on the initial condition and activation.

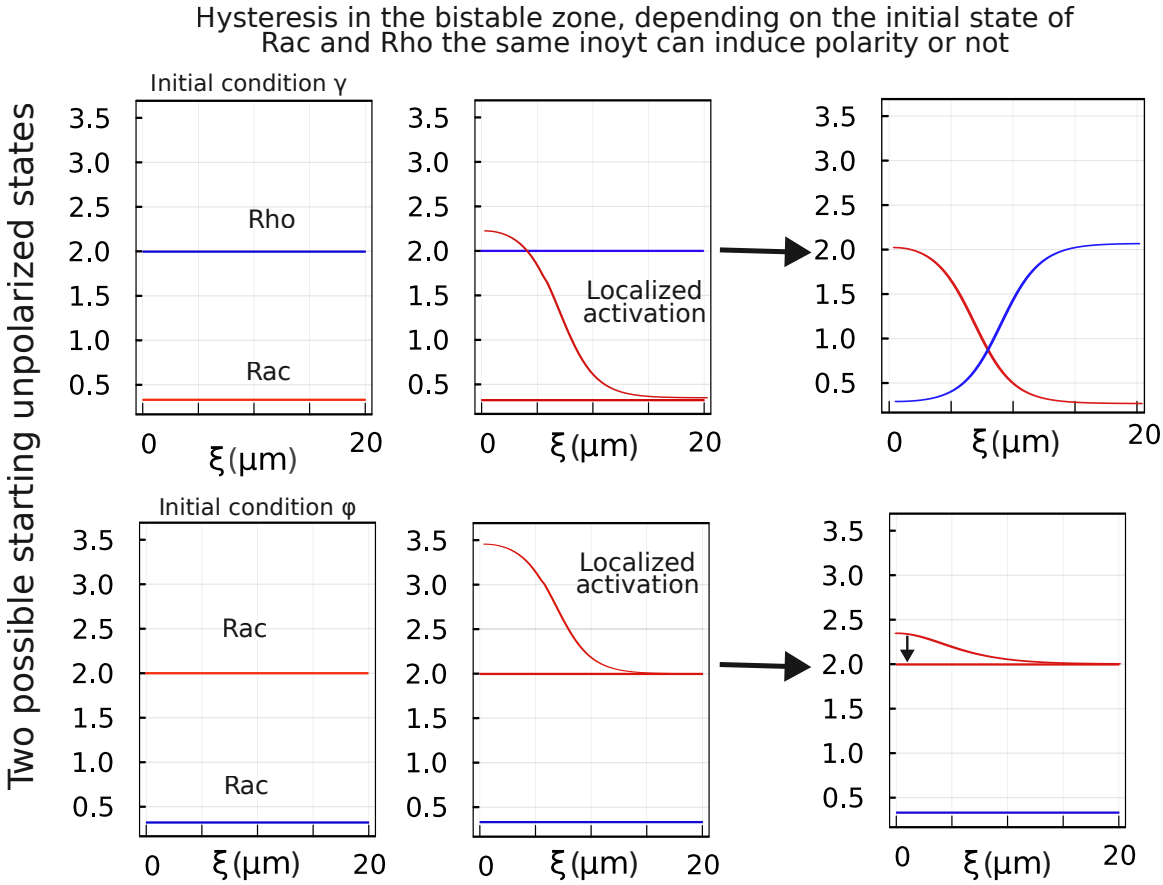


Figure 4: Representation of how the two possible configuration in the bistable region for $a$ and $b$, introduced with Figure 3, affects an optogenetic induced activation.

# 3 Mechanical model

## 3.1 Hypotheses

To describe the mechanics of the membrane - cortex interaction, we follow a previous composite model [7] that we expand to explicitly account for the inhomogeneous membrane-cortex attachment density (MCA) revealed experimentally (Supp Fig. 5A-D). The membrane mechanics is approximated to a linear elastic response at the macroscopic level, resisting effectively stretching or compressive stress through a membrane tension $\sigma$, which may hence be positive or negative. This effective tension is the result of the highly folded structure of the membrane, that results physically from a competition between thermal and active fluctuations, bending rigidity and compressive stress induced by cortical contraction. The cortex is modeled classically as a viscous and contractile shell-like material on the timescales of our experiments $t \simeq 100s$, described by a velocity $v$ and an active contractile stress $\sigma_a$. The membrane and cortex interact through MCA proteins, such as ezrin, that are firmly attached to the cortex in their active state but can flow within the membrane plane, that is tangentiallly fluid. The relative movement between the membrane and cortex results therefore in a friction term that is proportional to the relative velocity between the two surfaces and to to the local surface density of MCA proteins. We further account for the binding kinetics of MCA proteins from the membrane to the cortex and therefore distinguish the density of bound proteins $\rho_b$ from unbound density $\rho_u$. The binding of ERM MCA proteins such as ezrin is regulated by their phosphorylation state, it binds to the cortex in the active form and unbinds when it is dephosphorylated [14]. The model components are summarized in the sketch on Fig. 5.

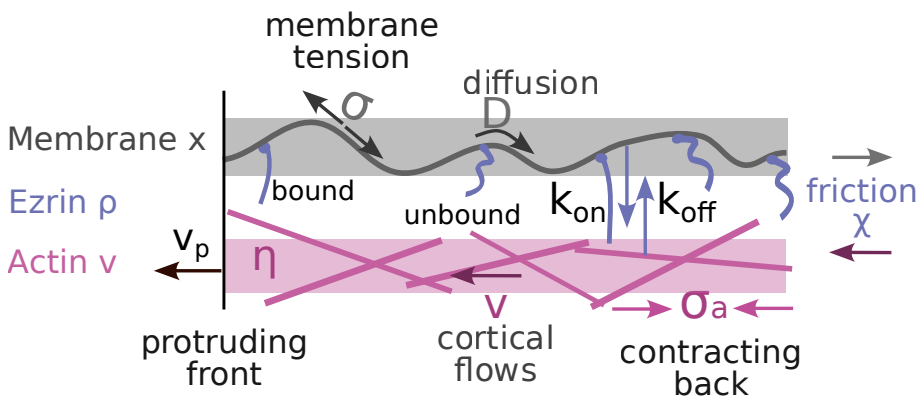


Figure 5: Representation of the mechanical model.

## 3.2 General equations

Let $x$ denote the membrane strain from its relaxed - or reference - state, and $\dot{x} = (\partial x)/(\partial t)$ its Eulerian velocity. We introduce $\xi\,[N.s.m^{-1}]$ the friction per bound ezrin protein in the membrane and $\sigma_0[N.m^{-1}]$ the two-dimensional membrane elastic modulus associated to its folding/unfolding, and which is homogeneous to a tension. The friction density per unit surface is given by $\rho_b\xi\,[N.s.m^{-3}]$, where $\rho_b\,[m^{-2}]$ is the surface density of bound ezrin proteins. Effective tangential force balance in the membrane reads

$$\sigma_0\nabla^2 x - \chi\rho_b\Big(\dot{x} - v\Big) = 0. \tag{14}$$

Let $v$ denote the local tangential velocity of the cortex. We introduce $\eta\,[N.s.m^{-1}]$ the two-dimensional effective viscosity of the cortex and $\sigma_a\,[N.m^{-1}]$ the two-dimensional active tension in the cortex, regulated by the local actomyosin contractility. Tangential force balance in the cortex reads

$$\eta\nabla^2 v + \nabla\sigma_a - \chi\rho_b\Big(v - \dot{x}\Big) = 0. \tag{15}$$

We note that the instantaneous local membrane tension may be defined from the local stretch as

$$\sigma = \sigma_0\nabla x \tag{16}$$

We furthermore introduce the conservation equations for bound and unbound MCA proteins $\rho_b$ and $\rho_u$ at the surface as

$$\frac{\partial \rho_b}{\partial t} + \nabla(v\rho_b) = k_{\text{on}}\rho_u - k_{\text{off}}\rho_b - \lambda_b\rho_b^3, \tag{17a}$$

$$\frac{\partial \rho_u}{\partial t} + \nabla\big(\dot{x}\rho_u\big) = D\nabla^2\rho_u - k_{\text{on}}\rho_u + k_{\text{off}}\rho_b, \tag{17b}$$

where we introduced the binding and unbinding rates $k_{\text{on}}\,[s^{-1}]$ and $k_{\text{off}}\,[s^{-1}]$, a two-dimensional diffusion coefficient $D\,[m.s^{-1}]$ for the unbound ezrin within the membrane plane and a non-linear saturation term for the bound protein density $\lambda_b$.

### 3.3 One-dimensional formulation

To simplify the description of the cortex-membrane interaction and exploiting the axisymmetry of the problem, we approximate in the following the system as a one-dimensional string of length $L$. We don't expect any of our results to be qualitatively different than with a more realistic 2D or 3D model of the surface. The composite surface deformation is described in one-dimension with respect to a spatial coordinate $\xi$, such that previous momentum and mass conservation equations read

$$\sigma_0\frac{\partial^2 x}{\partial \xi^2} - \chi\rho_b(\dot{x} - v) = 0, \tag{18a}$$

$$\eta\frac{\partial^2 v}{\partial \xi^2} + \nabla\sigma_a - \chi\rho_b\Big(v - \dot{x}\Big) = 0, \tag{18b}$$

$$\frac{\partial \rho_b}{\partial t} + \frac{\partial(v\rho_b)}{\partial \xi} = k_{\text{on}}\rho_u - k_{\text{off}}\rho_b - \lambda_b\rho_b^3, \tag{18c}$$

$$\frac{\partial \rho_u}{\partial t} + \frac{\partial(\dot{x}\rho_u)}{\partial \xi} = D\frac{\partial^2\rho_u}{\partial \xi^2} - k_{\text{on}}\rho_u + k_{\text{off}}\rho_b, \tag{18d}$$

These equations need to be complemented by appropriate boundary and intial conditions. We assume that the protrusive front can be modeled through a Dirichlet boundary conditions as a protrusive velocity $v_p$ for the cortex and a corresponding deformation due to protrusions for the membrane at $\xi = 0$. Since our one-dimensional system shall be seen as a representation of an axisymmetric mmembrane, "unwrapped" into a one-dimensional string, we furthermore impose zero Dirichlet boundary conditions for both the membrane strain and cortex velocity by symmetry at the opposite side of the cell (back) $\xi = L$:

$$v(\xi = 0) = v_p\,, \quad \text{and} \quad v(\xi = L) = 0 \tag{19}$$

$$x(\xi = 0) = \int_0^t v_p(t)\,dt.\,, \quad \text{and} \quad x(\xi = L) = 0 \tag{20}$$

One drawback of the simplified one-dimensional formulation is that the membrane may not relax even when the velocity reaches zero. To address this issue, we introduced an additional slow linear relaxation over time for $x(\xi = 0)$, accounting not only for protrusion retraction but also for other membrane relaxation mechanisms, such as membrane addition via endocytosis or exocytosis.

For ezrin surface density, we assume zero flux boundary conditions at membrane edges by symmetry again, which translate into zero Neumann boundary conditions at $\xi = 0$ and $\xi = L$

$$\frac{\partial \rho_b}{\partial \xi}\Big|_{0,L} = 0 \quad \text{and} \quad \frac{\partial \rho_u}{\partial \xi}\Big|_{0,L} = 0. \tag{21}$$

The initial values of bound and unbound densities are homogeneous and set such that their sum equals a conserved total number of ezrin proteins, defined as $M_\rho = \int(\rho_b + \rho_u)d\chi$, which allows us to define a characteristic mean ezrin density in one dimension

$$\rho_0 \equiv \frac{M_\rho}{L} \tag{22}$$

Unless specified, all other variables are set initially to their homogeneous basal or stationary values.

Although the parameters in the one-dimensional formulation of the model have different dimensions than their two-dimensional counterparts, the dimensionless parameters we will define further remain unchanged, and their numerical values can therefore be directly inferred from experimental measurements.

# 4 Mechanochemical model

## 4.1 Mechanochemical couplings

The mechanochemical model combines the local biochemical model for Rho and Rac described in Section 2 and the composite membrane-cortex mechanics described in Section 3. The control of Rho and Rac on cortical contractility and protrusion activity respectively are well described in the literature [15]. The feedbacks of mechanics on biochemical regulation are in contrary formulated based on experimental results from this manuscript.

**Cortical tension**
The dependence of the contractile tension on Rho concentration in the membrane is assumed to be linear:

$$\sigma_a = \sigma_a^0 \, \frac{b}{k_a}, \tag{23}$$

where $\sigma_a^0$ is a basal contractile tension in the cortex.

**Protrusive velocity**
For the protrusive activity, we assume that the protrusion velocity is activates with Rac and introduce a switch mechanism where protrusion occurs above a Rac concentration threshold $a_{\rm th}$ , while also accounting for the resistance exerted by membrane tension $\sigma$ [16]

$$v_p \simeq \frac{v_0}{(1+\sigma^2/\sigma_0^2)} \mathrm{th}\big(a - a_{\rm th}\big), \tag{24}$$

$$\mathrm{th}\big(a - a_{\rm th}\big) = \frac{1}{2}\Big[\tanh\Big(\frac{a - a_{\rm th}}{k_a}\Big) + 1\Big]. \tag{25}$$

**Rac activation**
Based on experimental results on Fig. 4, we furthermore assume that the Rac activation rate depends on the bound ezrin concentration $\rho_b$ in a switch like manner, where it is increased below a threshold value $\rho_{\rm th}$. We do not model explicitly stochastic blebbing and the competition for Pip2 for simplicity. The spatially-resolved equation for Rac dynamics is modified accordingly as follows

$$\frac{\partial a}{\partial t} = \Big(\alpha_0 + \alpha\, \mathrm{th}(\rho_b - \rho_{\rm th})\Big) \frac{k_a^2}{k_a^2 + b^2} - d_a a + D_a \nabla^2 a, \tag{26}$$

$$\text{where } \mathrm{th}(\rho_b - \rho_{\rm th}) = \frac{1}{2}\Big[1 - \tanh\Big(\frac{\rho_b - \rho_{\rm th}}{\rho_0}\Big)\Big], \tag{27}$$

where we introduced a membrane diffusion coefficient $D_a$ for Rac, a basal value $\rho_0$ for the ezrin surface density that will be defined later, and an additional activation rate $\alpha$ for the dependence on ezrin.

**Rho activation**
Based on experimental results on Fig. 2E-L, we finally assume that the Rho activation rate depends on the membrane tension $\sigma$ in a switch like manner, where it is increased above a threshold value $\sigma_{\rm th}$. The spatially-resolved equation for Rho dynamics is modified accordingly as follows

$$\frac{\partial b}{\partial t} = \Big(\beta_0 + \beta\, \mathrm{th}(\sigma - \sigma_{th})\Big) \frac{k_b^2}{k_b^2 + a^2} - d_b b + D_b \nabla^2 b \tag{28}$$

$$\text{where } \mathrm{th}(\sigma - \sigma_{\rm th}) = \frac{1}{2}\Big[\tanh\Big(\frac{\sigma - \sigma_{\rm th}}{\sigma_0}\Big) + 1\Big], \tag{29}$$

where we introduced a membrane diffusion coefficient $D_b$ for Rho, and an additional activation rate $\beta$ for the dependence on membrane tension.

## 4.2 Coupled dynamic equations

The full mechanochemical model has six dynamical variables $a$, $b$, $v$, $x$, $\rho_b$ and $\rho_u$, the dynamics of which is governed by six partial differential equations

$$\frac{\partial a}{\partial t} = \Big(\alpha_0 + \alpha\,\mathrm{th}(\rho_b - \rho_{\mathrm{th}})\Big)\frac{k_a^2}{k_a^2 + b^2} - d_a a + D_a \nabla^2 a, \tag{30a}$$

$$\frac{\partial b}{\partial t} = \Big(\beta_0 + \beta\,\mathrm{th}(\sigma - \sigma_{th})\Big)\frac{k_b^2}{k_b^2 + a^2} - d_b b + D_b \nabla^2 b, \tag{30b}$$

$$\sigma_0 \nabla^2 x - \chi\,\rho_b\left(\dot{x} - v\right) = 0, \tag{30c}$$

$$\eta \nabla^2 v + \sigma_a^0 \nabla\left(\frac{b}{k_a}\right) - \chi\,\rho_b\left(v - \dot{x}\right) = 0, \tag{30d}$$

$$\frac{\partial \rho_b}{\partial t} + \nabla(v \cdot \rho_b) = k_{\mathrm{on}}\rho_u - k_{\mathrm{off}}\rho_b - \lambda_b \rho_b^3, \tag{30e}$$

$$\frac{\partial \rho_u}{\partial t} + \nabla\big(\dot{x} \cdot \rho_u\big) = -k_{\mathrm{on}}\rho_u + k_{\mathrm{off}}\rho_b + D\nabla^2 \rho_u, \tag{30f}$$

To these equations, one has to add the boundary conditions, which have been made explicit in one dimension in (20), (19), (21). Additional zero-flux boundary conditions for Rac and Rho surface density $a$ and $b$ can be expressed identically to those for $\rho_b$ and $\rho_u$ (21) as Neumann boundary conditions. Finally, the explicit coupling of the protrusion velocity with other variables is defined in (24).

## 4.3 Non-dimensionalization

We non-dimensionalize the previous equations as follows:

We set a basal contractile tension in the cortex $\sigma_a^0$, which allows us to non-dimensionalize the membrane tension and to define a characteristic timescale associated to the active-viscous cortex relaxation that will serve to non-dimensionalize all other times

$$\bar{\sigma}_0 = \frac{\sigma_0}{\sigma_a^0}, \quad \tau_a \equiv \frac{\eta}{\sigma_a^0}, \quad \bar{t} = \frac{t}{\tau_a}. \tag{31}$$

We define a hydrodynamic length $\lambda$ measuring the spatial extent of cortical viscous flows slowed down by friction and we non-dimensionalize all lengths by a characteristic size $L$ of the cell

$$\lambda \equiv \sqrt{\frac{\eta}{\chi\,\rho_0}}, \quad \bar{\lambda} = \frac{\lambda}{L}, \quad \bar{\xi} = \frac{\xi}{L}, \quad \bar{x} = \frac{x}{L}, \quad \bar{v} = v\frac{\tau_a}{L}. \tag{32}$$

Ezrin surface densities are non-dimensionalized using the mean density $\rho_0$ defined in (22)

$$\rho_b = \frac{\rho_b}{\rho_0}, \quad \bar{\rho}_u = \frac{\rho_u}{\rho_0}, \quad \bar{\lambda}_b = \lambda_b \frac{\rho^2}{k_{\mathrm{off}}} \tag{33}$$

We further define a dimensionless reaction rate constant as ratio of binding and unbinding rates and an effective Peclet number

$$K \equiv \frac{k_{\mathrm{on}}}{k_{\mathrm{off}}}, \quad \mathcal{P}e \equiv \frac{L}{\tau_a}\frac{L}{D} = \frac{v_a L}{D}, \tag{34}$$

where $v_a \equiv L/\tau_a$ is a basal advection velocity by cortical flows.

For Rac and Rho surface densities, we choose $k_a$ and $k_b$ as characteristic concentrations and non-dimensionalize other parameters using previously defined time and lengthscales

$$\bar{a} = \frac{a}{k_b}, \quad \bar{b} = \frac{b}{k_a}, \quad \bar{\alpha}_{(0)} = \frac{\alpha_{(0)}}{k_b\,d_a}, \quad \bar{\beta}_{(0)} = \frac{\beta_{(0)}}{k_a\,d_b}, \quad \bar{d}_{a,b} = d_{a,b}\tau_a, \quad \bar{D}_{a,b} = D_{a,b}\frac{\tau_a}{L^2}. \tag{35}$$

The resulting dimensionless set of equations become

$$\frac{1}{\bar{d}_a}\frac{\partial \bar{a}}{\partial \bar{t}} - \bar{D}_a \bar{\nabla}^2 a = \Big(\bar{\alpha}_0 + \bar{\alpha}\,\mathrm{th}(\bar{\rho}_b - \bar{\rho}_{th})\Big)\frac{1}{1+\bar{b}^2} - \bar{a} \tag{36a}$$

$$\frac{1}{\bar{d}_b}\frac{\partial \bar{b}}{\partial \bar{t}} - \bar{D}_b \bar{\nabla}^2 b = \Big(\bar{\beta}_0 + \bar{\beta}\,\mathrm{th}(\bar{\sigma} - \bar{\sigma}_{th})\Big)\frac{1}{1+\bar{a}^2} - \bar{b} \tag{36b}$$

$$\bar{\sigma}_0 \nabla^2 \bar{x} - \frac{1}{\bar{\lambda}^2}\bar{\rho}_b\left(\dot{\bar{x}} - \bar{v}\right) = 0 \tag{36c}$$

$$\bar{\nabla}^2 \bar{v} + \bar{\nabla}\bar{b} - \frac{1}{\bar{\lambda}^2}\bar{\rho}_b\big(\bar{v} - \dot{\bar{x}}\big) = 0 \tag{36d}$$

$$\frac{1}{\bar{k}_{\mathrm{off}}}\Big(\frac{\partial \bar{\rho}_b}{\partial \bar{t}} + \nabla(\bar{v}\cdot\bar{\rho}_b)\Big) = K\bar{\rho}_u - \bar{\rho}_b - \bar{\lambda}_b\,\bar{\rho}_b^3 \tag{36e}$$

$$\frac{1}{\bar{k}_{\mathrm{off}}}\Big(\frac{\partial \bar{\rho}_u}{\partial \bar{t}} + \nabla(\dot{\bar{x}}\cdot\bar{\rho}_u) - \frac{1}{\mathcal{P}e}\nabla^2\bar{\rho}_u\Big) = -K\bar{\rho}_u + \bar{\rho}_b \tag{36f}$$

# 5 Numerical Implementation

The equations are implemented using the finite-element method in a one-dimensional segment of size $L$, defined between the spatial coordinates $\xi = 0$ and $\xi = L$. The implementation is performed in the language *Julia* using the library *Gridap* [17, 18]. The code is available on a repository on Github.

We first present the weak formulation of the equations in one dimension and then the spatial and temporal discretization choices.

## 5.1 Weak formulation

The weak form is derived from the strong form of the dimensionless equations (36) by multiplying each equation by an arbitrary test function $w$ and integrating over the spatial domain. For simplicity, we omit the overbars typically used to denote dimensionless variables.

$$\int_0^L w(\xi,t)\left[\sigma_0\frac{\partial^2}{\partial\xi^2}x(\xi,t) - \frac{1}{\lambda^2}\rho_b(\xi,t)\big(\dot{x}(\xi,t) - v(\xi,t)\big)\right]d\xi = 0. \tag{37}$$

Integrating by parts we obtain

$$\begin{aligned}\int w\sigma_0\frac{\partial}{\partial\xi}\frac{\partial x}{\partial\xi}d\xi \quad &= \int k\,\tfrac{\partial}{\partial\xi}\Big(w\tfrac{\partial x}{\partial\xi}\Big)\partial\xi - \int \tfrac{1}{\lambda^2}\tfrac{\partial x}{\partial\xi}\cdot\tfrac{\partial w}{\partial\xi}d\xi \\ &= \sigma_0\Big(w\tfrac{\partial x}{\partial\xi}\Big)\Big|_0^L - \int k\,\tfrac{\partial x}{\partial\xi}\cdot\tfrac{\partial w}{\partial\xi}d\xi\end{aligned} \tag{38}$$

The last line (38) corresponds the weak formulation of the problem.
Similarly for the cortex mechanics equation, we start from the integral

$$\int_0^L w\Big[\eta\frac{\partial^2 v}{\partial\xi^2} + \frac{\partial\sigma_a}{\partial\xi} - \chi\,\rho_b(\xi)\Big(v - \dot{x}\Big)\Big]d\xi = 0 \tag{39}$$

and will split the $\nabla^2$ by integration by parts

$$\int w\,\eta\nabla^2 v\,d\xi = -\int \eta\nabla w\nabla v\,d\xi + \Big(w\eta\nabla v\Big)\Big|_0^L. \tag{40}$$

Repeating the process for all the equations while taking adimensional equations, the system of weak equations is

$$\sigma_0\Big(w\nabla x\Big)\Big|_0^L - \int\Big[\sigma_0\nabla x\nabla w - w\,\frac{1}{\lambda^2}\,\rho_b\,\dot{x}\Big]d\xi = -\int w\,\frac{1}{\lambda^2}\,\rho_b v\,d\xi \tag{41a}$$

$$\Big(w\nabla v\Big)\Big|_0^L - \int\Big[\nabla w\nabla v - w\,\frac{1}{\lambda^2}\,\rho_b\,v\Big]d\xi = -\int\Big[w\,\nabla b + w\,\frac{1}{\lambda^2}\,\rho_b\,\dot{x}\Big]d\xi \tag{41b}$$

$$\int w\Big[\frac{1}{k_{\text{off}}}\Big(\frac{\partial \rho_b}{\partial t} + \nabla(v\cdot\rho_b)\Big) + \rho_b + \lambda_b \rho_b^3\Big] d\xi = \int w\, K\, \rho_u\, d\xi \tag{41c}$$

$$-\frac{1}{k_{\text{off}}\mathcal{P}e}\Big(w\nabla\rho_u\Big)\Big|_0^L + \int\Big(\frac{1}{k_{\text{off}}\mathcal{P}e}\nabla\rho_u\cdot\nabla w + w\Big[\frac{1}{k_{\text{off}}}\Big(\frac{\partial\rho_u}{\partial t} + \nabla(\dot{x}\cdot\rho_u)\Big) + K\,\rho_u\Big]\Big)d\xi = \int w\,\rho_b\,d\xi \tag{41d}$$

$$-D_a\Big(w\nabla a\Big)\Big|_0^L \int\Big(D_a\nabla a\cdot\nabla w + w\Big[\frac{1}{d_a}\frac{\partial a}{\partial t} + a\Big]\Big)d\xi = \int w\Big[\Big(\alpha_0 + \alpha\,\text{th}(\rho_b - \rho_{th})\Big)\frac{1}{1+b^2}\Big]d\xi, \tag{41e}$$

$$-D_b\Big(w\nabla b\Big)\Big|_0^L \int\Big(D_b\nabla b\cdot\nabla w + w\Big[\frac{1}{d_b}\frac{\partial b}{\partial t} + b\Big]\Big)d\xi = \int w\Big[\Big(\beta_0 + \beta\,\text{th}(\sigma - \sigma_{th})\Big)\frac{1}{1+a^2}\Big]d\xi. \tag{41f}$$

Here we separate the terms depending on the variable we will solve in the left hand-side from the other terms in the right hand-side.

## 5.2 Spatial discretization

We use a cartesian discretisation and a scalar-valued Lagrangian finite elements space of order 1.

## 5.3 Temporal discretization

The weak form of the partial differential equations (PDEs) above are solved in space at a given time. Time discretization for each variable $y$ is implemented as a simple forward Euler time-stepping

$$\frac{\partial y}{\partial t} \approx \frac{y_t - y_{t-1}}{\Delta t}, \tag{42}$$

where $\Delta t$ is the time-step.

We chose the time-step $\Delta t$ small enough to ensure proper convergence of the solutions of our equations. A range from $10^{-2}$s to $10^{2}$s was studied and we determined that 1s allows for good numerical accuracy while maintaining computational time acceptable.

## 5.4 Parameters numerical values

There is a wide array of parameters to be set up in this model, which will be summarized here. The membrane tension $\sigma_0$ [N/m] can be measured from membrane tether pulling [19, 7]. The friction coefficient is estimated as $\mu = \chi\rho_0$, where $\chi \approx 10^{-6}$ Pa.s.m [20] is the drag coefficient for an individual linker within the membrane and $\rho = 10^{14}m^{-2}$ is a typical surface density of linkers [21].

| Notation | Quantity | Experimental Value | Ref(s). |
|---|---|---|---|
| $L = R\,\pi$ | Neutrophil cell half perimeter | $20\mu$m | |
| $\sigma_0$ | Membrane tension | 10 pN/$\mu$m | [19] |
| $\eta_{3D}$ | Actomyosin viscosity | $10^4 - 10^5$Pa s | [10] |
| $\mu$ | Friction coefficient | 100 pN.s/$\mu m^3$ | [20, 21] |
| $T_0$ | Cortex thickness | 200nm | [22] |
| $\eta = \eta_{3D}T_0$ | 2D cortical viscosity | $10^5$ pN.s/$\mu$m | |
| $D$ | Diffusion of ezrin on the membrane | 0.003 $\mu$m$^2$/s | [23] |
| $k_{\text{on}}$ | Rate of ezrin binding | 5.0 1/s | [23] |
| $k_{\text{off}}$ | Rate of ezrin unbinding | 1.4 1/s | [23] |
| $\bar{\alpha}_0$ | Dimensionless rate of Rac activation | 0.1-10 | |
| $\beta_0$ | Dimensionless rate of Rho activation | 0.1-10 | |
| $d_a$ | Rate of Rac deactivation | 0.04 1/s | |
| $d_b$ | Rate of Rho deactivation | 0.04 1/s | |

**Table of values used for the different mechanical parameters.**

# References


[1] M. Otsuji, S. Ishihara, C. Co, K. Kaibuchi, A. Mochizuki, and S. Kuroda, "A mass conserved reaction–diffusion system captures properties of cell polarity," *PLoS computational biology*, vol. 3, no. 6, p. e108, 2007.

[2] Y. Mori, A. Jilkine, and L. Edelstein-Keshet, "Wave-pinning and cell polarity from a bistable reaction-diffusion system," *Biophysical journal*, vol. 94, no. 9, pp. 3684–3697, 2008.

[3] C. Zmurchok, D. Bhaskar, and L. Edelstein-Keshet, "Coupling mechanical tension and gtpase signaling to generate cell and tissue dynamics," *Physical biology*, vol. 15, no. 4, p. 046004, 2018.

[4] K. H. Kopfer, W. Jäger, and F. Matthäus, "A mechanochemical model for rho gtpase mediated cell polarization," *Journal of theoretical biology*, vol. 504, p. 110386, 2020.

[5] L. K. Nguyen, B. N. Kholodenko, and A. Von Kriegsheim, "Rac1 and rhoa: Networks, loops and bistability," *Small GTPases*, vol. 9, no. 4, pp. 316–321, 2018.

[6] A. Jilkine, A. F. Marée, and L. Edelstein-Keshet, "Mathematical model for spatial segregation of the rho-family gtpases based on inhibitory crosstalk," *Bulletin of mathematical biology*, vol. 69, pp. 1943–1978, 2007.

[7] H. De Belly, S. Yan, H. B. da Rocha, S. Ichbiah, J. P. Town, P. J. Zager, D. C. Estrada, K. Meyer, H. Turlier, C. Bustamante *et al.*, "Cell protrusions and contractions generate long-range membrane tension propagation," *Cell*, vol. 186, no. 14, pp. 3049–3061, 2023.

[8] G. Salbreux, J. Prost, and J.-F. Joanny, "Hydrodynamics of cellular cortical flows and the formation of contractile rings," *Physical review letters*, vol. 103, no. 5, p. 058102, 2009.

[9] M. Mayer, M. Depken, J. S. Bois, F. Jülicher, and S. W. Grill, "Anisotropies in cortical tension reveal the physical basis of polarizing cortical flows," *Nature*, vol. 467, no. 7315, pp. 617–621, 2010.

[10] H. Turlier, B. Audoly, J. Prost, and J.-F. Joanny, "Furrow constriction in animal cell cytokinesis," *Biophysical journal*, vol. 106, no. 1, pp. 114–123, 2014.

[11] Z. Shi, Z. T. Graber, T. Baumgart, H. A. Stone, and A. E. Cohen, "Cell membranes resist flow," *Cell*, vol. 175, no. 7, pp. 1769–1779, 2018.

[12] T. S. Gardner, C. R. Cantor, and J. J. Collins, "Construction of a genetic toggle switch in escherichia coli," *Nature*, vol. 403, no. 6767, pp. 339–342, 2000.

[13] A. R. Houk, A. Jilkine, C. O. Mejean, R. Boltyanskiy, E. R. Dufresne, S. B. Angenent, S. J. Altschuler, L. F. Wu, and O. D. Weiner, "Membrane tension maintains cell polarity by confining signals to the leading edge during neutrophil migration," *Cell*, vol. 148, no. 1, pp. 175–188, 2012.

[14] R. G. Fehon, A. I. McClatchey, and A. Bretscher, "Organizing the cell cortex: the role of erm proteins," *Nature reviews Molecular cell biology*, vol. 11, no. 4, pp. 276–287, 2010.

[15] C. D. Nobes and A. Hall, "Rho gtpases control polarity, protrusion, and adhesion during cell movement," *The Journal of cell biology*, vol. 144, no. 6, pp. 1235–1244, 1999.

[16] D. Raucher and M. P. Sheetz, "Cell spreading and lamellipodial extension rate is regulated by membrane tension," *The Journal of cell biology*, vol. 148, no. 1, pp. 127–136, 2000.

[17] S. Badia and F. Verdugo, "Gridap: An extensible finite element toolbox in julia," *Journal of Open Source Software*, vol. 5, no. 52, p. 2520, 2020. [Online]. Available: https://doi.org/10.21105/joss.02520

[18] F. Verdugo and S. Badia, "The software design of gridap: A finite element package based on the julia JIT compiler," *Computer Physics Communications*, vol. 276, p. 108341, Jul. 2022. [Online]. Available: https://doi.org/10.1016/j.cpc.2022.108341

[19] P. Sens and J. Plastino, "Membrane tension and cytoskeleton organization in cell motility," *Journal of Physics: Condensed Matter*, vol. 27, no. 27, p. 273103, 2015.

[20] F. Brochard-Wyart, N. Borghi, D. Cuvelier, and P. Nassoy, "Hydrodynamic narrowing of tubes extruded from cells," *Proceedings of the National Academy of Sciences*, vol. 103, no. 20, pp. 7660–7663, 2006. [Online]. Available: https://www.pnas.org/doi/abs/10.1073/pnas.0602012103

[21] R. Alert, J. Casademunt, J. Brugués, and P. Sens, "Model for probing membrane-cortex adhesion by micropipette aspiration and fluctuation spectroscopy," *Biophysical journal*, vol. 108, no. 8, pp. 1878–1886, 2015.

[22] A. G. Clark, K. Dierkes, and E. K. Paluch, "Monitoring actin cortex thickness in live cells," *Biophysical journal*, vol. 105, no. 3, pp. 570–580, 2013.

[23] M. Fritzsche, R. Thorogate, and G. Charras, "Quantitative analysis of ezrin turnover dynamics in the actin cortex," *Biophysical journal*, vol. 106, no. 2, pp. 343–353, 2014.